

Measurement of the cross-correlation angular power spectrum between the stochastic gravitational wave background and galaxy overdensity

Kate Z. Yang^{1,*}, Jishnu Suresh², Giulia Cusin,^{3,4} Sharan Banagiri^{5,1}, Noelle Feist,¹ Vuk Mandic¹,
Claudia Scarlata,¹ and Ioannis Michaloliakos⁶

¹University of Minnesota, School of Physics and Astronomy, Minneapolis, Minnesota 55455, USA


²Centre for Cosmology, Particle Physics and Phenomenology (CP3), Université Catholique de Louvain, Louvain-la-Neuve, B-1348, Belgium

³Sorbonne Université, CNRS, UMR 7095, Institut d'Astrophysique de Paris, 75014 Paris, France

⁴Université de Genève, Département de Physique Théorique and Centre for Astroparticle Physics, 24 quai Ernest-Ansermet, CH-1211 Genève 4, Switzerland

⁵Center for Interdisciplinary Exploration and Research in Astrophysics, Northwestern University, 1800 Sherman Avenue, Evanston, Illinois 60201, USA

⁶Department of Physics, University of Florida, Gainesville, Florida 32611, USA

 (Received 17 May 2023; accepted 27 July 2023; published 23 August 2023)

We study the cross-correlation between the stochastic gravitational-wave background (SGWB) generated by binary black hole mergers across the Universe and the distribution of galaxies across the sky. We use the anisotropic SGWB measurement obtained using data from the third observing run (O3) of Advanced LIGO detectors and galaxy overdensity obtained from the Sloan Digital Sky Survey spectroscopic catalog. We compute, for the first time, the angular power spectrum of their cross-correlation. Instead of integrating the SGWB across frequencies, we analyze the cross-correlation in 10-Hz-wide SGWB frequency bands to study the frequency dependence of the cross-correlation angular power spectrum. Finally, we compare the observed cross-correlation to the spectra predicted by astrophysical models. We apply a Bayesian formalism to explore the parameter space of the theoretical models, and we set constraints on a set of (effective) astrophysical parameters describing the galactic process of gravitational-wave (GW) emission. Parametrizing with a Gaussian function the astrophysical kernel describing the local process of GW emission at galactic scales, we find the 95% upper limit on kernel amplitude to be $2.88 \times 10^{-32} \text{ erg cm}^{-3} \text{ s}^{-1/3}$ when ignoring the shot noise in the GW emission process and $2.52 \times 10^{-32} \text{ erg cm}^{-3} \text{ s}^{-1/3}$ when the shot noise is included in the analysis. As the sensitivity of the LIGO-Virgo-KAGRA network improves, we expect to be able to set more stringent bounds on this kernel function and constrain its parameters.

DOI: [10.1103/PhysRevD.108.043025](https://doi.org/10.1103/PhysRevD.108.043025)

I. INTRODUCTION

The first three observing runs of Advanced LIGO [1], Advanced Virgo [2], and KAGRA [3] gravitational-wave (GW) detectors have resulted in detections of nearly a hundred mergers of compact binary systems [4]: binary black holes (BBHs), binary neutron stars (BNSs), and binary systems composed of one neutron star and one black hole (NSBH). These discoveries have enabled a series of investigations including measurements of the rate and distributions of these binary systems [5], tests of general relativity [6], independent measurements of the Hubble constant [7], tests of the neutron star equation of state [8], and others. This trend is expected to continue in the

upcoming observation runs O4 and O5 [9] of LIGO, Virgo, and KAGRA.

One of the prime targets of the upcoming observing runs will be the stochastic gravitational-wave background (SGWB), which arises as a superposition of uncorrelated signals of many different GW sources [10,11]. The SGWB is expected to include contributions from many different production processes in the early Universe, including models of amplification of primordial tensor vacuum fluctuations [12–15], inflationary models that include backreaction of gauge fields [16,17], parametric resonances in the preheating stage following inflation [18], models of additional “stiff” energy components in the early Universe [19], phase transition models [20–26], and cosmic (super)string models [27–37]. On the other hand, the SGWB of astrophysical origin is given by the superposition of GW signals emitted by different populations of astrophysical sources, from the onset of stellar activity until today. In the frequency band of current

*yang5991@umn.edu

Earth-based observatories, sources include BBH, BNS, and NSBH systems [38–45], rotating neutron stars [42,46–50], and supernovae [11,51–57].

Both cosmological and astrophysical SGWB components are expected to be anisotropic. A primary source of anisotropy in the received flux is due to the anisotropic distribution of emitting sources and the anisotropic emission process. A secondary source of anisotropy is due to propagation: even if a given SGWB component is isotropic at the time of emission, anisotropies are created due to the fact that GW signals propagate in a Universe where cosmic structures are present and, hence, they feel the effects of the gravitational potential of matter structures (in the form of lensing, time delay, integrated time delay; see e.g. [58–60]). We also note that kinematic anisotropies are expected, due to the relative motion of our rest frame on Earth with respect to the emission rest frame [61,62].

This raises a distinct possibility that the SGWB energy density is correlated with the anisotropy in other (electromagnetic) observables, such as galaxy counts (GCs), gravitational (weak) lensing, cosmic microwave background, cosmic infrared background, and others. Measurements of these correlations would provide new ways to study the distribution of matter in our Universe and its evolution.

Typical cosmological SGWB components are expected to have the same level of anisotropy as the cosmic microwave background (CMB): a scale-invariant angular power spectrum $\ell(\ell+1)C_\ell \propto \text{const}$, where ℓ parametrizes the angular scale, and a level of anisotropy of the order of $\sim 10^{-5}$ with respect to the monopole [63]. In contrast, extragalactic astrophysical SGWBs have a scaling given by clustering, resulting in $(\ell+1)C_\ell \propto \text{const}$, and a higher level of anisotropy, at the level of $\sim 10^{-2}$ with respect to the monopole [59,60,64–74].

While most of the cosmological SGWB components are expected to be stationary and continuous over the observation time (hence representing *irreducible* background components), the astrophysical background in the frequency band of ground-based detectors is expected to have *popcornlike nature* due to the discreteness of emissions in time. As a consequence, the angular power spectrum of the SGWB from mergers of compact binaries has an important Poisson shot-noise component, which adds to the clustering one [65,70,71,74]. Formally, the total SGWB angular power spectrum is given by $C_\ell^{\text{tot}} = C_\ell + N^{\text{shot}}$, where the first term on the right-hand side is the contribution from clustering while the second component represents shot noise. This latter term is flat in ℓ space (it is just an offset) and it is expected to dominate over the clustering contribution; see [65,70,71,74]. Even though shot noise contains astrophysical information, it does not provide any information about the spatial distribution of sources. A possible way to overcome this problem, i.e. to separate the clustering part from the shot noise, is to consider cross-correlations between a SGWB map and electromagnetic

tracers of structure, such as galaxy distributions [74]. In addition to serving as independent observables of structure in the Universe, cross-correlations provide one with powerful SGWB anisotropy detection tools, as they typically have a higher signal-to-noise ratio (SNR) than the SGWB autocorrelation—see e.g. [64,65,74–76] in the context of the extragalactic astrophysical background. We are aware that cross-correlating EM tracers with individual events of compact binary coalescence is also used, such as in the calculation of the Hubble constant H_0 [77].

In this paper, we focus on correlations between the SGWB (as measured in the recent observing runs of Advanced LIGO, Advanced Virgo, and KAGRA) and the distribution of galaxies across the sky [from the Sloan Digital Sky Survey (SDSS)]. We assume that the dominant background components in the ~ 100 Hz band is coming from mergers of extragalactic compact objects, and we use the astrophysical model of Refs. [64,65,69] to describe the galactic process of GW emission. We compute the corresponding angular power spectrum of the cross-correlation, and we compare it with the angular power spectrum extracted from data. Our final goal is to perform a parameter estimation: we introduce an effective parametrization for the astrophysical model describing GW production and propagation, and we study the constraints that can be set on these effective model parameters from a comparison with data. We stress that the methods developed here can also be applied to cross-correlations between SGWB and other electromagnetic tracers of structure in the Universe.

The paper is structured as follows. In Sec. II we will review the model predictions for the angular power spectrum of the cross-correlation between SGWB and the galaxy counts distribution. In Sec. III, we will present the frequency-dependent anisotropic SGWB search results using the latest data from terrestrial GW detectors. In Sec. IV we review the galaxy catalog that will be used in our study, namely from the Sloan Digital Sky Survey. In Sec. V we present the measured SGWB-GC angular power spectra. In Sec. VI we use the measured angular power spectra to make estimates of model parameters introduced in Sec. II. A discussion and our final remarks are presented in Sec. VII.

II. MODELING SGWB-GALAXY COUNT ANGULAR POWER SPECTRA

A. Astrophysical models of angular power spectra

The observed GW energy density parameter Ω_{GW} is defined as the background energy density ρ_{GW} per units of logarithmic frequency f and solid angle \mathbf{e} , normalized by the critical density of the Universe today ρ_c . It can be divided into an isotropic background contribution $\bar{\Omega}_{\text{GW}}$ and a contribution from anisotropic perturbations $\delta\Omega_{\text{GW}}$ [59,60,65]:

$$\Omega_{\text{GW}}(\mathbf{e}, f) = \frac{f}{\rho_c} \frac{d^3 \rho_{\text{GW}}}{d^2 \mathbf{e} df}(\mathbf{e}, f) = \frac{\bar{\Omega}_{\text{GW}}(f)}{4\pi} + \delta\Omega_{\text{GW}}(\mathbf{e}, f), \quad (2.1)$$

where the isotropic background spectrum can be written as the integral over conformal distance r (where we treat speed of light $c = 1$):

$$\bar{\Omega}_{\text{GW}}(f) = \int dr \partial_r \bar{\Omega}_{\text{GW}}(f, r), \quad (2.2)$$

$$\partial_r \bar{\Omega}_{\text{GW}}(f, r) = \frac{f}{\rho_c} \mathcal{A}(f, r), \quad (2.3)$$

and the function $\mathcal{A}(f, r)$ is an astrophysical kernel that contains information on the local production of GWs at galaxy scales. Schematically this kernel can be parametrized as [74]

$$\mathcal{A}(f, r) = \frac{a^4}{4\pi} \int d\mathcal{L}_{\text{GW}} \bar{n}_G(\mathcal{L}_{\text{GW}}, r) \mathcal{L}_{\text{GW}}, \quad (2.4)$$

where a is the Universe scale factor and \bar{n}_G is the average physical number density of galaxies at distance r with gravitational-wave luminosity \mathcal{L}_{GW} . Different astrophysical models give quite different predictions for this kernel; see e.g. [65] for an explorative approach. For the SGWB due to mergers of compact objects such as BBH and BNS, the low-frequency band ($f \lesssim 100$ Hz) is dominated by the inspiral phase contributions and follows a simple power law $\Omega_{\text{GW}} \sim f^{2/3}$. Looking at predictions of different astrophysical models (see e.g. [65,69]), one can recognize some common features in the redshift dependence of the kernel which in first approximation can be captured by the following Gaussian parametrization:

$$\mathcal{A}(f, z) = \mathcal{A}(f) e^{-(z-z_c)^2/2\sigma_z^2} = A_{\text{max}} f^{-1/3} e^{-(z-z_c)^2/2\sigma_z^2}, \quad (2.5)$$

where we used $z = z(r)$ to express the astrophysical kernel as a function of redshift and frequency. In Fig. 1 we present the astrophysical kernel as a function of redshift for several representative frequencies in the band of terrestrial GW detectors [65]. When making use of the parametrization in Eq. (2.5), we have three parameters in total $\theta = (A_{\text{max}}, z_c, \sigma_z)$: kernel amplitude A_{max} , peak redshift z_c , and peak width σ_z . Typically the peak of the astrophysical kernel follows the peak of star formation rate (i.e. $z_c \lesssim 1$) and the width σ_z depends on the astrophysical model chosen and is typically of the order $\sigma_z \sim 0.5$; see [65] for details. As we can see in Fig. 1, the Gaussian approximation is valid for redshifts between 0 and 2. This applies to our analysis below which extends up to $z = 0.8$.

Since $\delta\Omega_{\text{GW}}$ is a stochastic quantity, it can correlate with other cosmological stochastic observables. An interesting

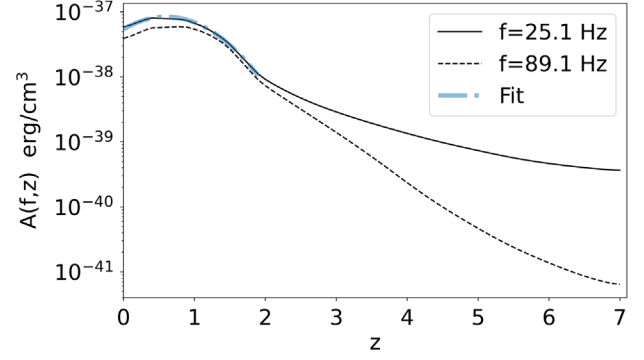


FIG. 1. Astrophysical kernel for the astrophysical model used as a reference in Ref. [65], as function of redshift and for frequencies 25.1 and 89.1 Hz, with a power-law-Gaussian fit of $A_{\text{max}} = 4 \times 10^{-37} \text{ erg cm}^{-3} \text{ s}^{-1/3}$, $z_c = 0.6$, $\sigma_z = 0.9$.

observable to look at is the cross-correlation of the SGWB with the distribution of galaxies, i.e. with the galaxy number counts Δ defined as the overdensity of the number of galaxies per unit of redshift and solid angle

$$\Delta(\mathbf{e}, z) \equiv \frac{N(z, \mathbf{e}) - \bar{N}(z)}{\bar{N}(z)}. \quad (2.6)$$

First, if astrophysical GW sources are located in galaxies, we would expect the SGWB and the galaxy distribution to have a high correlation level. Second, cross-correlating with galaxies helps to mitigate the problem of shot noise and to possibly extract the clustering information out of the shot-noise threshold [65,70,71,74]. Finally, by cross-correlating with the galaxy distribution at different redshifts, one could try to get a tomographic reconstruction of the redshift distribution of sources. In this article, to maximize the SNR of the cross-correlation we do not bin the galaxy distribution in redshift, but we rather integrate the number counts (2.6) over the redshift range covered by our catalog.

The angular power spectrum of the GW and galaxy count autocorrelations and for their cross-correlations are defined as

$$(2\ell + 1)C_\ell^{\text{GW}}(f; \theta) \equiv \sum_{m=-\ell}^{\ell} \langle a_{\ell m}(f; \theta) a_{\ell m}^*(f; \theta) \rangle, \quad (2.7)$$

$$(2\ell + 1)C_\ell^{\text{GC}} \equiv \sum_{m=-\ell}^{\ell} \langle b_{\ell m} b_{\ell m}^* \rangle, \quad (2.8)$$

$$(2\ell + 1)C_\ell^{\text{cross}}(f; \theta) \equiv \sum_{m=-\ell}^{\ell} \langle a_{\ell m}(f; \theta) b_{\ell m}^* \rangle, \quad (2.9)$$

where the bracket denotes an ensemble average and $a_{\ell m}(f)$ and $b_{\ell m}$ are the coefficients of the spherical harmonics decomposition of the SGWB energy density and galaxy number counts, respectively. Explicitly

$$\begin{aligned}\delta\Omega_{\text{GW}}(\mathbf{e}, f; \theta) &= \sum_{\ell=0}^{\infty} \sum_{m=-\ell}^{\ell} a_{\ell m}(f; \theta) Y_{\ell m}(\mathbf{e}), \\ \Delta(\mathbf{e}) &= \sum_{\ell=0}^{\infty} \sum_{m=-\ell}^{\ell} b_{\ell m} Y_{\ell m}(\mathbf{e}).\end{aligned}\quad (2.10)$$

It can be shown that the angular power spectra of the auto- and cross-correlation are given by [59]

$$C_{\ell}^{\text{GW}}(f; \theta) = \frac{2}{\pi} \int dk k^2 |\delta\Omega_{\text{GW}, \ell}(k, f; \theta)|^2, \quad (2.11)$$

$$C_{\ell}^{\text{GC}} = \frac{2}{\pi} \int dk k^2 |\Delta_{\ell}(k)|^2, \quad (2.12)$$

$$C_{\ell}^{\text{cross}}(f; \theta) = \frac{2}{\pi} \int dk k^2 \delta\Omega_{\text{GW}, \ell}^*(k, f; \theta) \Delta_{\ell}(k), \quad (2.13)$$

where k is the wave number. Keeping only the leading-order contribution to the anisotropy given by clustering (neglecting line of sight effects), we have

$$\delta\Omega_{\text{GW}, \ell}(k, f; \theta) = \frac{f}{4\pi\rho_c} \int dr \mathcal{A}(r, f; \theta) [b(r) \delta_{m,k}(r) j_{\ell}(kr)], \quad (2.14)$$

where j_{ℓ} are spherical Bessel functions, while δ_m is the dark-matter overdensity, related to galaxy overdensity via the bias factor that we assume to be scale independent and with redshift evolution given by $b(z) = b_0 \sqrt{1+z}$ and $b_0 = 1.5$ [78,79]. The corresponding contribution from galaxy overdensities reads

$$\Delta_{\ell}(k) = \int dr W(r) [b(r) \delta_{m,k}(r) j_{\ell}(kr)], \quad (2.15)$$

where $W(r)$ is a window function normalized to one which selects the redshift bin in the galaxy catalog we want to

$$\left(\frac{S}{N}\right)_{\text{cross}}^2 = \sum_{\ell} \frac{(2\ell+1) C_{\ell}^{\text{cross}}}{(C_{\ell}^{\text{cross}} + N_{\text{shot}}^{\text{cross}})^2 + (C_{\ell}^{\text{GW}} + N_{\text{shot}}^{\text{GW}})(C_{\ell}^{\text{GC}} + N_{\text{shot}}^{\text{GC}})}, \quad (2.17)$$

where C_{ℓ}^{GW} and $N_{\text{shot}}^{\text{GW}}$ denote the angular power spectrum and the shot noise of the SGWB map, respectively, while C_{ℓ}^{GC} and $N_{\text{shot}}^{\text{GC}}$ are the angular power spectrum and shot noise of the galaxy map (we have suppressed their dependencies on parameters θ). The three noise contributions are given by [74]

$$N_{\text{shot}}^{\text{GW}}(\theta) = \left(1 + \frac{1}{\beta_T}\right) \left(\frac{f}{4\pi\rho_c}\right)^2 \int \frac{dr}{r^2} \frac{1}{a^3 \bar{n}_G} \mathcal{A}^2(r, f; \theta), \quad (2.18)$$

consider in the cross-correlations. As already mentioned, in our analysis we do not bin in redshift in order to maximize the SNR; hence, the function $W(r)$ extends to the entire redshift range of the galaxy catalog.

B. Shot noise

Up to now, in our description of GW sources we implicitly introduced two assumptions: we assumed that astrophysical sources are located in galaxies, distributed in space as a continuous field, and we assumed that the GW emission is continuous and stationary over the observation time. However, when considering the SGWB due to BBH mergers, the realization of the BBH mergers during the observation period is subject to Poisson (shot, or popcorn) noise in both space and time [70,74]. This shot noise introduces additional angular structure in both the SGWB and the galaxy distribution and therefore has to be accounted for in both the prediction of C_{ℓ} 's (GW, GC, and cross) and in their covariance matrices. As shown in Ref. [74], the shot-noise contribution to the cross-correlation angular power spectrum is independent of ℓ but still dependent on astrophysical parameters $\theta = (A_{\text{max}}, z_c, \sigma_z)$. That is, the shot noise offsets the clustering values given in Eq. (2.11):

$$C_{\ell}^{\text{cross, tot}}(\theta) = C_{\ell}^{\text{cross}}(\theta) + N_{\text{shot}}^{\text{cross}}(\theta). \quad (2.16)$$

Hence, while shot noise may (partly) mask the clustering contribution, it still carries astrophysical information that can be measured. Further, as discussed in detail in Ref. [74], the shot noise associated with the cross-correlation is much smaller than the one associated with the SGWB autocorrelation, which is why cross-correlating is a very promising method to get a first detection of the SGWB anisotropy. Indeed, assuming that shot noise is the only noise component (i.e. considering a perfect instrument with infinite sensitivity) one has that the SNR of the cross-correlation scales as [74]

$$N_{\text{shot}}^{\text{cross}}(\theta) = \frac{f}{4\pi\rho_c} \int \frac{dr}{r^2} \frac{1}{a^3 \bar{n}_G} W(r) \mathcal{A}(r, f; \theta), \quad (2.19)$$

$$N_{\text{shot}}^{\text{GC}} = \int \frac{dr}{r^2} \frac{1}{a^3 \bar{n}_G} W^2(r), \quad (2.20)$$

where $a^3 \bar{n}_G$ is the comoving number density of galaxies and we defined

$$\beta_T \equiv \frac{T}{a^3 \bar{n}_G} \frac{d^2 \mathcal{N}}{dV dt}, \quad (2.21)$$

where T is the observation time and $d^2 \mathcal{N}/dV dt$ denotes the local merger rate. To get these expressions we have assumed a monochromatic GW luminosity function and that all galaxies emit GWs.

To get an estimate for the prefactor (2.21), we can use the observed local rate of BBH mergers, $d^2 \mathcal{N}/dV dt \sim 100 \text{ Gpc}^{-3} \text{ yr}^{-1}$. This estimate for the merger rate, which neglects the contribution of BNS mergers, provides a lower bound for the total merger rate in the $\sim 100 \text{ Hz}$ band and hence leads to a conservative estimate for the GW shot noise. We also assume a constant comoving galaxy density $a^3 \bar{n}_G \sim 0.1 \text{ Mpc}^{-3}$. For LIGO-Virgo-KAGRA O3, the observation time period $T \sim 1 \text{ yr}$, so finally $\beta_T \sim 10^{-6}$. This leads to a large prefactor $\propto \beta_T^{-1}$ when evaluating the shot noise for the GW map [Eq. (2.18)], much larger than the ones of cross-correlation and of galaxies alone. Since the denominator of Eq. (2.17) scales linearly with the GW shot noise $N_{\text{shot}}^{\text{GW}}$ (as opposed to scaling quadratically in the SNR of SGWB autocorrelation), the SNR of the cross-correlation is typically much larger than the one of the SGWB autocorrelation (see [74] for a detailed analysis).

III. MEASUREMENT OF SGWB ANGULAR POWER SPECTRA

In this section, we review how the SGWB anisotropy is measured using GW data. We use the publicly available folded dataset [80,81] from the third observing run (O3) of Advanced LIGO detectors located in Hanford, Washington and Livingston, Louisiana. In order to capture the frequency dependence of the model presented in Sec. II, we analyze the data in 10 Hz frequency bands and build an unbiased estimator of the SGWB angular power spectrum.

A. Basic concepts: Dirty and clean maps

From an observational point of view, a SGWB is typically estimated by cross-correlating the output of two different detectors located at two different points on Earth and assuming that the noise and the noise signal in the two detectors are not correlated.

Assuming that the SGWB is unpolarized, Gaussian, and stationary, the quadratic expectation value of the GW strain $h_A(f, \mathbf{e})$ across different sky positions and frequencies can be expressed as

$$\langle h_A^*(f, \mathbf{e}) h_{A'}(f', \mathbf{e}') \rangle = \frac{1}{4} P(f, \mathbf{e}) \delta_{AA'} \delta(f - f') \delta(\mathbf{e}, \mathbf{e}'), \quad (3.1)$$

where A denotes the GW polarization and $P(f, \mathbf{e})$ encodes the contribution from all parts of the sky and frequency to the total SGWB. Given these assumptions, one can express the anisotropy of the SGWB as

$$\Omega_{\text{GW}}(f, \mathbf{e}) = \frac{f}{\rho_c} \frac{d^3 \rho_{\text{GW}}}{df d^2 \mathbf{e}} = \frac{2\pi^2 f^3}{3H_0^2} P(f, \mathbf{e}), \quad (3.2)$$

where H_0 is the Hubble constant taken to be $H_0 = 67.4 \text{ kms}^{-1} \text{ Mpc}^{-1}$ [82]. In what follows, we further assume that Ω_{GW} can be factorized into frequency- and direction-dependent terms by separating $P(f, \mathbf{e})$ as¹ [83,84]

$$P(f, \mathbf{e}) = P(\mathbf{e})H(f). \quad (3.3)$$

In our analysis, we model the spectral dependence $H(f)$ as a power law:

$$H(f) = \left(\frac{f}{f_{\text{ref}}} \right)^{\alpha-3}, \quad (3.4)$$

where α is the spectral index and f_{ref} denotes a reference frequency. Throughout this analysis, we set the reference frequency to 25 Hz and choose the power-law index $\alpha = 2/3$ as predicted for a compact binary coalescence SGWB. The angular distribution $P(\mathbf{e})$ can be expanded in terms of any set of basis functions defined on the two-sphere. The choice of this basis will not affect the physical search results. However, to reduce the computational burden and ease the interpretation of the results, one usually chooses either pixel or spherical harmonic basis for the analysis, depending on the sky distribution of sources. A spherical harmonic (SpH) basis is suitable for searching for a diffuse background considered in this work. In SpH basis, one can expand the anisotropy map over the basis functions $Y_{\ell m}$ as

$$P(\mathbf{e}) = \sum_{\ell=0}^{\ell_{\text{max}}} \sum_{m=-\ell}^{\ell} P_{\ell m} Y_{\ell m}(\mathbf{e}). \quad (3.5)$$

We will discuss the choice of ℓ_{max} below. Following the maximum-likelihood (ML) method for mapping the GW anisotropy [83,85], a standard ML solution for $P(\mathbf{e})$ in SpH basis can be written as (in the limit of low signal-to-noise ratio)

$$\hat{P}_{\ell m} = \sum_{\ell', m'} (\Gamma^{-1})_{\ell m, \ell' m'} \hat{X}_{\ell' m'}, \quad (3.6)$$

where

$$\hat{X}_{\ell m} = \sum_t \sum_f \gamma_{\ell m}(f, t) \frac{H(f)}{P_1(f, t) P_2(f, t)} \hat{C}(f, t), \quad (3.7)$$

¹The factorization does not amount to a loss of generality when conducting stochastic search analysis in small frequency bands, as we expect the signal to have a smooth power spectral profile.

$$\Gamma_{\ell m, \ell' m'} = \sum_t \sum_f \gamma_{\ell m}^*(f, t) \frac{H^2(f)}{P_1(f, t) P_2(f, t)} \gamma_{\ell' m'}(f, t), \quad (3.8)$$

where $\hat{C}(f, t)$ is the cross-correlation spectrum computed by multiplying Fourier transforms of the strain time series from the two GW detectors used in the analysis [83]. The summation is done over time segments denoted by t (typically data is divided into short segments, each lasting 1–3 min) and over frequency bins denoted by f (typically 1/4 or 1/32 Hz binning is used). As discussed below, we will repeat the analysis in 10-Hz-wide bands, summing over all frequency bins between 20 and 30 Hz, 30 and 40 Hz, etc.

The quantity $\hat{X}_{\ell m}$ is usually referred to as the *dirty map* (it represents the SGWB sky seen through the response matrices of a baseline created by a pair of detectors) whereas the $\Gamma_{\ell m, \ell' m'}$ is called the *Fisher information matrix* (it encodes the uncertainty associated with the dirty map measurement). In both equations, $P_i(f, t)$ is the noise power spectral density of detector i , and $\gamma_{\ell m}$ captures the geometrical factors associated with the two geographically separated detectors with different orientations (usually referred to as the overlap reduction function [83,86]).

The observed $\hat{P}_{\ell m}$, the *clean map*, obtained through the *deconvolution* shown in Eq. (3.6) is an unbiased estimator of the angular distribution of the SGWB, $\langle \hat{P}_{\ell m} \rangle = P_{\ell m}$. It is also worth noting that, in the weak-signal limit, one can show that

$$\begin{aligned} \langle \hat{X}_{\ell m} \hat{X}_{\ell' m'}^* \rangle - \langle \hat{X}_{\ell m} \rangle \langle \hat{X}_{\ell' m'}^* \rangle &\approx \Gamma_{\ell m, \ell' m'}, \\ \langle \hat{P}_{\ell m} \hat{P}_{\ell' m'}^* \rangle - \langle \hat{P}_{\ell m} \rangle \langle \hat{P}_{\ell' m'}^* \rangle &\approx (\Gamma^{-1})_{\ell m, \ell' m'}. \end{aligned} \quad (3.9)$$

The above equation implies that $\Gamma_{\ell m, \ell' m'}$ is the covariance matrix of the dirty map, and $(\Gamma^{-1})_{\ell m, \ell' m'}$ is the covariance matrix of the clean map. In particular, since the dirty map is obtained by averaging over many time segments and frequency bins, by the central limit theorem the resulting $\hat{X}_{\ell m}$'s are multivariate Gaussian variables with zero means and the covariance matrix given by $\Gamma_{\ell m, \ell' m'}$. Further, since the clean map is obtained by a linear transformation of the dirty map [cf. Eq. (3.6)], the $\hat{P}_{\ell m}$'s are also multivariate Gaussian variables with zero means and the covariance matrix given by $(\Gamma^{-1})_{\ell m, \ell' m'}$.

One can then introduce an estimator for the SGWB angular power spectrum, which describes the angular scale of structure in the clean map as

$$\hat{C}_\ell = \frac{1}{2\ell + 1} \sum_{m=-\ell}^{\ell} |\hat{P}_{\ell m}|^2. \quad (3.10)$$

We will see in the next section that this estimator is biased, and we will describe how one can obtain an unbiased estimator from it. Also, note that by conducting the analysis

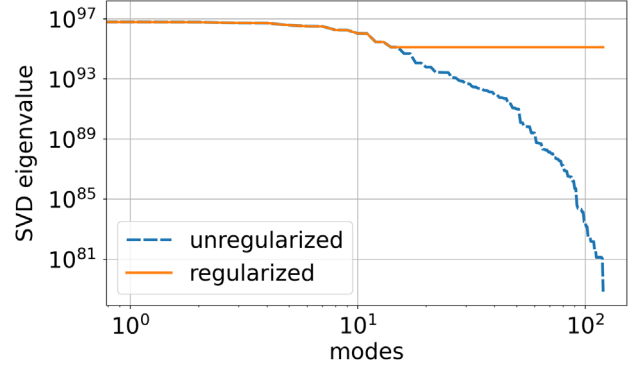


FIG. 2. SVD eigenvalues of the Fisher matrix in the 20–30 Hz band are shown. Regularization of the Fisher matrix is accomplished by replacing eigenvalues smaller than S_{\min} with S_{\min} , where S_{\min} is defined to be 10^{-2} of the maximum eigenvalue and is depicted by the horizontal part of the orange line.

in narrow frequency bands (10 Hz wide in our case), these estimators will encode frequency dependence.

B. Unbiased regularized estimator

In practice, due to the existence of blind directions in GW detector response, the SGWB searches are often insensitive to certain ℓm modes. Consequently, Fisher matrices are often singular and cannot be inverted. Therefore we use a regularized pseudoinverse, which conditions the original matrix to circumvent other numerical errors, to obtain our estimators. One can employ different regularization techniques to perform this pseudoinversion [83,87–89]. One of the most common regularization procedures used in the literature is the singular value decomposition (SVD) technique. In the SVD procedure one can decompose $\Gamma_{\ell m, \ell' m'}$ (which is a Hermitian matrix) as

$$\Gamma = USV^*, \quad (3.11)$$

where U and V are unitary matrices and S is a diagonal matrix whose nonzero elements are the positive and real eigenvalues of the Fisher matrix. Then the problematic ℓm modes will correspond to the smallest elements of S . To illustrate the general nature of these eigenvalues, we have plotted the relative size of the eigenvalues for a typical Fisher matrix (computed from the 20–30 Hz GW dataset with $\ell_{\max} = 10$) in Fig. 2. Then to condition the ill-conditioned matrix, a threshold on the eigenvalue (S_{\min}) is chosen. The choice is made by considering the proper trade-off between the quality of the deconvolution and the increase in numerical noise from less sensitive modes.² Any values below this cutoff are considered too small, and one can replace them either with

²It is worth noting that the regularization problem becomes severe as one considers smaller frequency bands. A proper trade-off between the variance of the estimator and the subsequent biases needs to be thoroughly explored in such cases.

infinity or with the smallest eigenvalue above the cutoff. Throughout this work, we will set the threshold S_{\min} to be 10^2 times smaller than the largest eigenvalue; all eigenvalues smaller than S_{\min} are replaced by S_{\min} . These choices and the subsequent regularized eigenvalues are also illustrated in Fig. 2.

Given the regularized inverse Fisher matrix Γ_R^{-1} , the ML solution in Eq. (3.6) takes the form [83,85]

$$\hat{\mathbf{p}}_{\ell m}^R = \sum_{\ell', m'} (\Gamma_R^{-1})_{\ell m, \ell' m'} \hat{X}_{\ell' m'}, \quad (3.12)$$

still obeying multivariate Gaussian distribution. The covariance matrix of this clean map (under weak-signal approximation) also takes a slightly different form compared to the one given in Eq. (3.9). It can be written as (we have dropped the indices for the Fisher matrix for simplicity)

$$K_{\ell m, \ell' m'} = \langle \hat{\mathbf{p}}_{\ell m}^R \hat{\mathbf{p}}_{\ell' m'}^{R*} \rangle - \langle \hat{\mathbf{p}}_{\ell m}^R \rangle \langle \hat{\mathbf{p}}_{\ell' m'}^{R*} \rangle = \Gamma_R^{-1} \Gamma \Gamma_R^{-1}. \quad (3.13)$$

From the expectation value and uncertainty in the estimators defined in Eq. (3.9), one can show that the regularized SGWB angular power spectrum estimators obey

$$\langle \hat{C}_{\ell}^R \rangle \approx C_{\ell} + \frac{1}{2\ell + 1} \sum_m (\Gamma_R^{-1})_{\ell m, \ell m}, \quad (3.14)$$

$$\langle (\hat{C}_{\ell}^R)^2 \rangle - \langle \hat{C}_{\ell}^R \rangle^2 \approx \frac{2}{(2\ell + 1)^2} \sum_{mm'} |(\Gamma_R^{-1})_{\ell m, \ell m'}|^2. \quad (3.15)$$

One can see from the expressions of estimators of the clean map and the angular power spectra that both depend on inverting the Fisher information matrix $\Gamma_{\ell m, \ell' m'}$. Thus, our estimators are biased. The unbiased estimators of the SGWB angular power spectrum are given by

$$\hat{C}'_{\ell} = \hat{C}_{\ell} - \frac{1}{2\ell + 1} \sum_m (\Gamma_R^{-1})_{\ell m, \ell m}. \quad (3.16)$$

C. Choice of ℓ_{\max}

The choice of ℓ_{\max} in the expansion in Eq. (3.5) is ultimately determined by the detector sensitivity and the frequency dependence of the searched SGWB model [89]. However, when the Fisher matrix is ill defined, the regularization procedure introduces a bias that increases with ℓ_{\max} . In particular, larger ℓ_{\max} implies a larger Fisher matrix, regularization of a larger number of eigenvalues, and hence larger bias.

One way to assess this is to examine the diagonal entries of the Fisher and regularized inverse Fisher matrices, as in Fig. 3. The Fisher matrix diagonal elements decrease significantly as ℓ increases for the same m . If the Fisher matrix could be inverted, the diagonal elements of the

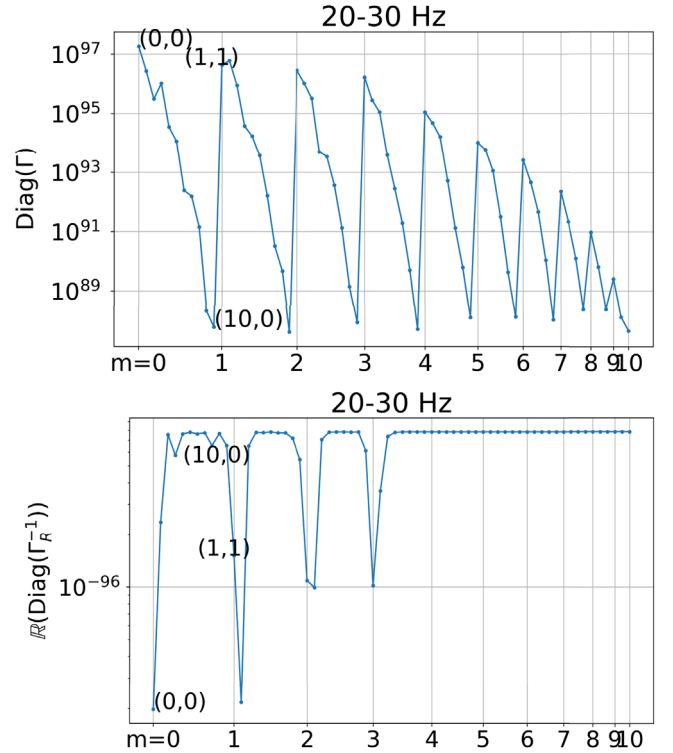


FIG. 3. Diagonal entries of the SGWB Fisher matrix and its inverse Fisher matrix (real part only) are shown for the 20–30 Hz band, with regularization defined in the text. The indices along the x axis are $(\ell, m) = (0, 0), (1, 0), \dots, (\ell_{\max}, 0), (1, 1), \dots, (\ell_{\max}, 1), \dots, (\ell_{\max} - 1, \ell_{\max} - 1), (\ell_{\max}, \ell_{\max})$, with $\ell_{\max} = 10$.

inverse Fisher matrix would correspondingly increase with ℓ for a fixed m . Figure 3 (bottom) indeed shows this increasing trend, but the trend saturates (reaches a plateau) after $\ell = 5$ because of the regularization. Propagating this to K in Eq. (3.13) implies that the covariance matrix for the clean map could have artificially low values (implying artificially good sensitivity) if one uses too large value of ℓ_{\max} . We therefore choose $\ell_{\max} = 5$ in our analysis to avoid this regularization bias.

D. Final angular power spectrum estimator

We note that the definition of the SGWB anisotropy in the theoretical model of Sec. II [cf. Eq. (2.10)] and in the SGWB search formalism [Eqs. (3.2)–(3.4)] have different normalizations. To build estimators that are directly compatible with the model prediction [Eq. (2.7)], note that the frequency dependence of the angular power defined in the SGWB search is [cf. Eqs. (3.2)–(3.4)]:

$$\mathcal{K} \equiv \frac{2\pi^2 f^3}{3H_0^2} \left(\frac{f}{f_{\text{ref}}} \right)^\alpha. \quad (3.17)$$

We can then define frequency-dependent estimators of the spherical harmonic coefficients of the clean map, whose

expectation values are consistent with their theoretical counterparts in Eq. (2.10):

$$\hat{a}_{\ell m}(f) = \mathcal{K} \hat{P}_{\ell m}. \quad (3.18)$$

The covariance matrix for these coefficients is given by a similar scaling:

$$K_{\ell m, \ell' m'}^{\text{GW}} = \mathcal{K}^2 K_{\ell m, \ell' m'}. \quad (3.19)$$

We then introduce the properly normalized, frequency-dependent estimators of the SGWB angular power spectrum:

$$\hat{C}_{\ell}^{\text{GW}}(f) = \frac{1}{2\ell + 1} \sum_{m=-\ell}^{\ell} |\hat{a}_{\ell m}(f)|^2. \quad (3.20)$$

Referring to Eq. (3.16), the unbiased angular power spectrum of the SGWB autocorrelation is then

$$\hat{C}_{\ell}^{\text{GW}}(f) = \hat{C}_{\ell}^{\text{GW}}(f) - \frac{\mathcal{K}^2}{2\ell + 1} \sum_m (\Gamma_R^{-1})_{\ell m, \ell m}. \quad (3.21)$$

We apply these definitions to the publicly available folded dataset [80,81] from the third observing run (O3) of Advanced LIGO detectors located in Hanford, Washington (H) and Livingston, Louisiana (L). We perform the analysis in 10 Hz frequency bands from 20 to 100 Hz with $\ell_{\text{max}} = 5$ and use the PYSTOCH pipeline [90,91] to compute the unbiased $\hat{C}_{\ell}^{\text{GW}}$ estimators of the angular power spectra and the corresponding $\hat{a}_{\ell m}$. The $\hat{C}_{\ell}^{\text{GW}}$ estimators and their variance [calculated from Eq. (3.15) times \mathcal{K}^2] in these frequency bands are shown in Fig. 4, as a function of ℓ for different frequencies and as a function of frequency for various values of the multipole ℓ (top and bottom panels, respectively). This figure shows that the SGWB auto power in all frequency bins and at all ℓ 's is consistent with zero at 2σ , implying there is no evidence for an anisotropic SGWB in these data. Note that the error bars increase at higher frequencies, which is a consequence of the lower strain sensitivity of LIGO detectors at higher frequencies and of the power-law frequency dependence in Eq. (3.17). It is worth noting here that the SGWB auto power and the error bars are consistent with the noise as in the case of results published in Ref. [92]. It is not straightforward to have a one-to-one comparison, given our analysis is performed in 10 Hz frequency bands in contrast to the broadband one shown in Ref. [92]. However, the SGWB auto power is in good agreement with the all-sky all-frequency SGWB angular power spectra shown in Ref. [93].

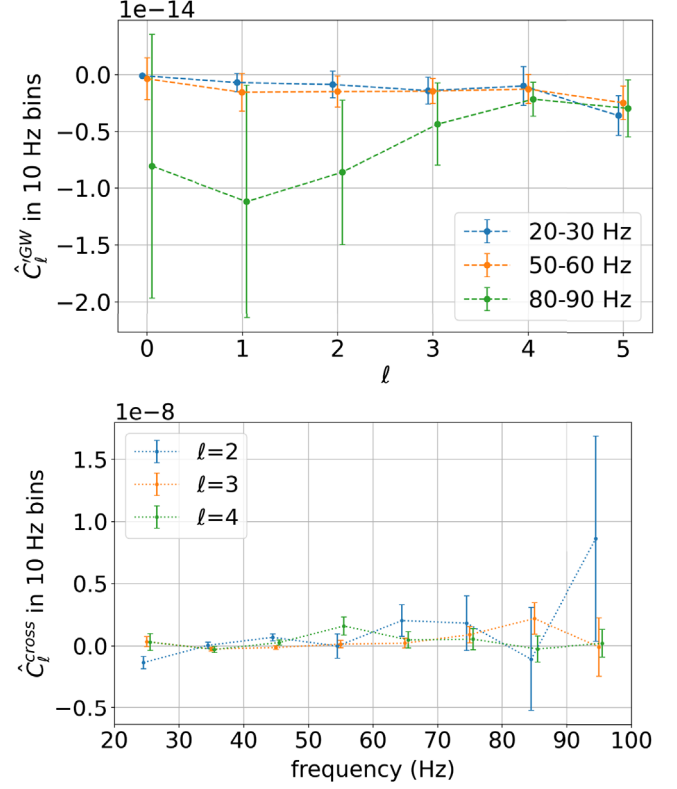


FIG. 4. Unbiased $\hat{C}_{\ell}^{\text{GW}}$ estimators with standard deviation error bars of the SGWB angular power spectrum are shown in 10-Hz-wide frequency bands (20–30, 50–60, and 80–90 Hz) as a function of ℓ (top) and as a function of frequency for $\ell = 2, 3, 4$ (bottom).

IV. MEASUREMENT OF GALAXY OVERDENSITY ANGULAR POWER SPECTRA

In our study, we use the galaxy number count from SDSS [94] for computing the galaxy overdensity angular power spectra. The SDSS imaging data cover around $1.5 \times 10^4 \text{ deg}^2$, or one-third of the sky. Within the range of r -band magnitude between 17 and 21 ($17 < m_r \leq 21$), after removing quasars and stars, there are 52.4 million galaxies in its photometric catalog and 2.8 million galaxies in its spectroscopic catalog. We remove stripe No. 82, which is scanned many more times compared to other stripes in the survey and is hence much brighter. This leaves us with 43.4 and 1.7 million galaxies in the two catalogs, respectively.

We use the galaxies in the SDSS spectroscopic catalog, whose redshift range extends to 0.8, with a median redshift of 0.39. We address systematic issues in the survey following [75]. In particular, we select only galaxies with r band seeing < 1.5 and extinction < 0.13 . Galaxy counts in pixels that are affected by these data quality cuts are replaced by the average galaxy counts of the remaining unaffected neighboring pixels. This leads to the final sky map of the galaxy number count in HEALPix-based

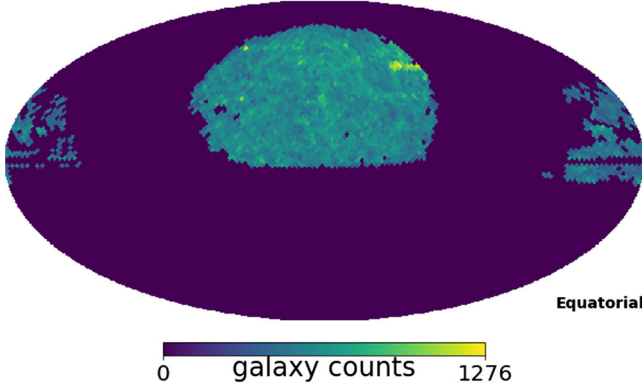


FIG. 5. Galaxy number count sky map in equatorial coordinates from the SDSS spectroscopic catalog. We have selected galaxies with r -band magnitude between 17 and 21 after removing quasars and stars and applied a mask to correct for systematics. The color bar stands for galaxy count in each HEALPix basis pixel with resolution of $N_{\text{side}} = 32$.

representation [95], with the systematic effects accounted for. This sky map is shown in equatorial coordinates in Fig. 5. The pixels with information cover around 20% of the full sky.

Based on this galaxy count sky map, we calculate the galaxy overdensity as a function of the sky direction and expand it in spherical harmonics as defined in Eq. (2.10). To account for the pixels with missing information, we apply a binary mask to the galaxy overdensity sky map in pixel basis, where we mask out every pixel without information (due to no observations or high systematics), before applying the spherical harmonic transformation. The obtained spherical harmonic coefficient estimators, $\hat{b}_{\ell m}$'s, are then used to compute the angular power spectrum for the galaxy overdensity autocorrelation:

$$\hat{C}_{\ell}^{\text{GC}} = \frac{1}{f_{\text{sky}}} \frac{1}{2\ell + 1} \sum_{m=-\ell}^{\ell} |\hat{b}_{\ell m}|^2. \quad (4.1)$$

Here, the factor f_{sky} denotes the fraction of the sky covered by the survey and is needed to account for the missing power in the sky map when performing the spherical harmonic transformation. We note that the same scaling must also be applied when computing the cross-correlation angular power spectrum between SGWB and GC partial-sky maps. The resulting GC angular power spectrum of the SDSS spectroscopic catalog is shown in Fig. 6, including uncertainties defined by the cosmic variance. The maximum ℓ used in this figure is determined by the angular resolution in Fig. 5 and is larger than the maximum ℓ obtained from the SGWB analysis above. Furthermore, due to the partial-sky coverage, there is a lower limit on ℓ that can be estimated as $\ell_{\text{min}} = \pi/\theta$, where θ is the spot size in the sky in radians. Hence we will use $\ell \geq 2$ for the SDSS spectroscopic catalog sky map (Fig. 5).

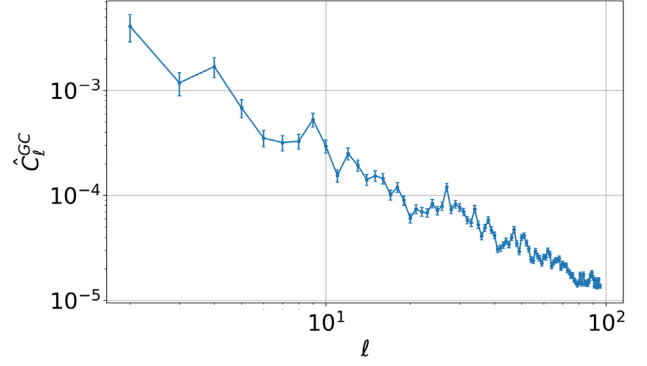


FIG. 6. The angular power spectrum $\hat{C}_{\ell}^{\text{GC}}$ for galaxy count overdensity, corrected for the partial-sky coverage, from the SDSS spectroscopic catalog of $2 \leq \ell \leq 95$. Uncertainties associated with the cosmic variance are shown.

V. MEASUREMENT OF CROSS-CORRELATION ANGULAR POWER SPECTRA

We now introduce an unbiased estimator for the angular power spectrum of the cross-correlation. We use the frequency-dependent SGWB multipoles $\hat{a}_{\ell m}(f)$ (estimated in 10 Hz frequency bins and introduced in Sec. III D) and the SDSS sky map multipoles, $\hat{b}_{\ell m}$, introduced in Sec. IV. We define the estimator of their cross-correlation angular power spectrum as

$$\hat{C}_{\ell}^{\text{cross}} = \frac{1}{f_{\text{sky}}} \frac{1}{2\ell + 1} \sum_{m=-\ell}^{\ell} \hat{b}_{\ell m}^* \hat{a}_{\ell m}. \quad (5.1)$$

As noted above, the $1/f_{\text{sky}}$ factor accounts for the incomplete sky coverage of the SDSS survey. To compute the covariance of this estimator, K_C , we assume that the galaxy map multipoles have much smaller uncertainties than their SGWB counterparts. This is a safe assumption since each pixel in the SDSS map in Fig. 5 counts thousands of galaxies (implying uncertainties at the level of a few percent), while the SGWB sky map is dominated by detector noise and shows no evidence of a signal. Consequently, Eq. (5.1) can be regarded as a linear transformation of the SGWB multipoles $\hat{a}_{\ell m}$, implying that the resulting $\hat{C}_{\ell}^{\text{cross}}$ are also multivariate Gaussian with the covariance matrix given by the appropriate propagation of the covariance of the SGWB multipoles K^{GW} :

$$(K_C)_{\ell, \ell'} = \frac{1}{f_{\text{sky}}^2} \frac{1}{(2\ell + 1)(2\ell' + 1)} \sum_{m, m'} \hat{b}_{\ell m}^* K_{\ell m \ell' m'}^{\text{GW}} \hat{b}_{\ell' m'}. \quad (5.2)$$

This covariance matrix does not take into account the cosmic variance or the shot noise contributions discussed in Sec. II B; cf. Eq. (2.17). Following Refs. [74,96], these contributions are diagonal and should be added to the above

covariance matrix. Our final covariance is therefore given by

$$(K_C^{\text{tot}})_{\ell\ell'} = (K_C)_{\ell\ell'} + \frac{\delta_{\ell\ell'}}{(2\ell+1)} \left[(C_\ell^{\text{GW}}(\theta) + N_{\text{shot}}^{\text{GW}}(\theta))(C_\ell^{\text{GC}} + N_{\text{shot}}^{\text{GC}}) + (C_\ell^{\text{cross}}(\theta) + N_{\text{shot}}^{\text{cross}}(\theta))^2 \right]. \quad (5.3)$$

We note that the shot noise is Poissonian in origin, so it can spoil the multivariate Gaussian nature of the $\hat{C}_\ell^{\text{cross}}$ estimators. In the limit when the cross-correlated signal is small, the shot-noise contribution to the covariance matrix will be relatively small compared to the SGWB instrumental noise contribution, and the distribution will be approximately Gaussian. This will be the case in our simulation analyses presented below. It is important to note, however, that as the SGWB instrumental noise improves and the cross-correlated signal becomes more significant, the shot-noise contribution will alter the $\hat{C}_\ell^{\text{cross}}$ distribution away from Gaussian. The parameter estimation scheme presented below will have to be correspondingly adapted.

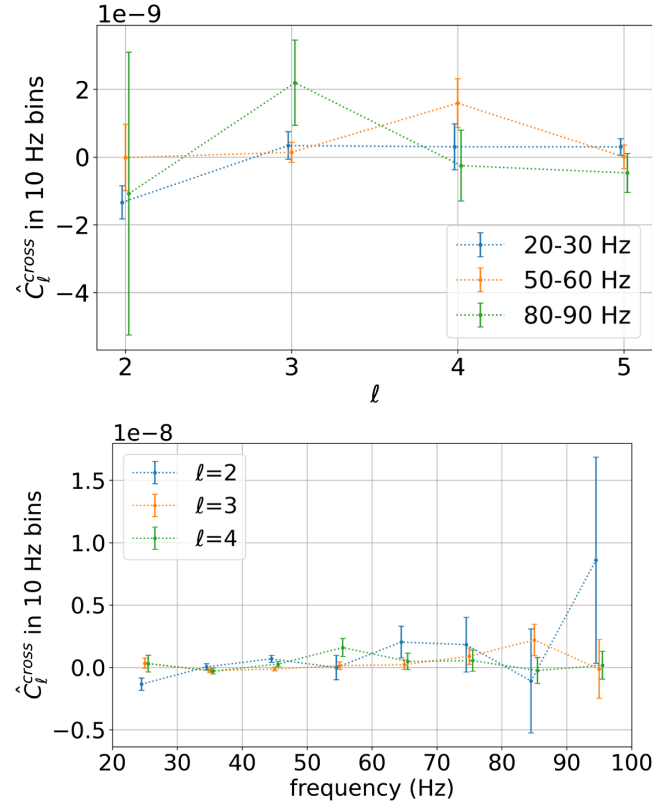


FIG. 7. Angular power spectra $\hat{C}_\ell^{\text{cross}}$ and standard deviation error bars of the cross-correlation between the measured SGWB sky maps (in 10-Hz-wide frequency bands) and the galaxy overdensity of the SDSS spectroscopic catalog, with $\ell \geq 2$ up to $\ell_{\text{max}} = 5$ are shown for several example frequency bands (top) and for several values of ℓ (bottom).

The angular power spectra of the cross-correlation between the measured SGWB sky maps (in 10 Hz width frequency bands from 20 to 100 Hz) and galaxy overdensity in the SDSS spectroscopic catalog are shown in Fig. 7. Error bars are also shown, defined as the square root of the diagonal terms of the K_C matrix, indicating no evidence for a cross-correlation signal. We observe that the noise level of cross-correlation $\hat{C}_\ell^{\text{cross}}$ increases with frequency. This is not surprising—in the absence of a cross correlation signal, the covariance of $\hat{C}_\ell^{\text{cross}}$ is given by the SGWB covariance in Eq. (5.2), which also increases with frequency; cf. Fig. 4.

VI. PARAMETER ESTIMATION

Having measured the angular power spectra $\hat{C}_\ell^{\text{cross}}$ of the cross-correlation between the SGWB sky maps and the galaxy overdensity of the SDSS spectroscopic catalog, we now turn our attention to extracting the astrophysical information from these measurements. We implement a Bayesian inference framework, where the posterior distribution of the astrophysical model parameters θ is given by

$$p(\theta | \hat{C}_\ell^{\text{cross}}) \propto \mathcal{L}(\hat{C}_\ell^{\text{cross}} | C_\ell^{\text{cross}}(\theta)) \pi(\theta), \quad (6.1)$$

where $\pi(\theta)$ denotes the prior distribution of the model parameters and \mathcal{L} denotes the likelihood of observing the data for given model parameters. As discussed above, in the limit when the cross-correlation signal is small, the $\hat{C}_\ell^{\text{cross}}$'s will approximately follow the multivariate Gaussian distribution with the covariance matrix given by either K_C if shot noise is ignored or by K_C^{tot} if shot noise is included. In particular, if shot noise is ignored,

$$\ln \mathcal{L}(\hat{C}_\ell | C_\ell(\theta)) = \frac{1}{2} \ln |K_C| - \frac{1}{2} (\hat{C}_\ell - C_\ell(\theta))^T K_C^{-1} (\hat{C}_\ell - C_\ell(\theta)). \quad (6.2)$$

Notice that here we are omitting the superscript “cross” to simplify the notation. If shot noise is included in the analysis, K_C is replaced by K_C^{tot} and $C_\ell(\theta)$ is modified as in Eq. (2.16). This likelihood is GW frequency dependent since it can be computed for each 10-Hz-wide band in the SGWB analysis. The overall likelihood is obtained by multiplying the likelihoods for individual frequency bands (or equivalently by summing up the individual log-likelihoods). Finally, since K_C does not depend on model parameters, the first term dependent on $|K_C|$ can be dropped. This is not the case when using K_C^{tot} , which depends on model parameters through the shot-noise terms in Eq. (5.3).

Our astrophysical model describing the galactic process of GW emission is given in Sec. II, with the shot-noise terms defined in Sec. II B. This model is parametrized by an astrophysical Gaussian kernel that has three parameters

$\theta = (A_{\max}, z_c, \sigma_z)$, with the Gaussian peak appearing near $z = 1$. Since the SDSS galaxy catalog used in our analysis extends only up to redshift $z \sim 0.8$, our analysis will not be able to assess the Gaussian peak: at small redshift, the kernel can be approximated by a linear function monotonically increasing with redshift [65]. In other words, the parameters z_c and σ_z will appear degenerate in our analysis, since increasing the mean z_c or decreasing the variance σ_z both result in a faster increase of the linear function. We, therefore, choose to fix $\sigma_z = 0.7$, which is compatible with the astrophysical model predictions, and our parameter space becomes two-dimensional: $\theta = (A_{\max}, z_c)$.

In the following analyses, we will scan the parameter space θ and compute the posterior distribution given by Eq. (6.1) using the measured $\hat{C}_\ell^{\text{cross}}$ presented in Sec. V, for both cases when we ignore the presence of shot noise and when we include the shot noise. These analyses will yield the first upper limits on the astrophysical kernel parameters. To demonstrate that our formalism correctly recovers the kernel parameters, and to study how inclusion of shot noise impacts the recovery, we will also perform recoveries of simulated signals. That is, we will choose parameters θ , compute the corresponding $C_\ell^{\text{cross}}(\theta)$'s and add them to the measured $\hat{C}_\ell^{\text{cross}}$. We will then repeat the calculation of the posterior distribution to recover the chosen θ parameters.

A. Results without shot noise

As a first step, we calculate the posterior distribution using the likelihood of Eq. (6.2), ignoring the shot-noise contribution (in both the signal and in the covariance matrix) and without adding any simulated signals. As noted above, we evaluate the likelihood in every 10-Hz-wide frequency bin between 20 and 100 Hz and then multiply these likelihoods to obtain the overall likelihood. We assume uniform prior distributions in the two parameters: $A_{\max} \in [1 \times 10^{-38}, 5 \times 10^{-32}] \text{ erg cm}^{-3} \text{ s}^{-1/3}$ and $z_c \in [0, 1]$ [65]. These ranges are both astrophysically well motivated and consistent with the sensitivity of our $\hat{C}_\ell^{\text{cross}}$ measurements. We define a uniform linear grid in this parameter space and evaluate the model C_ℓ 's, the likelihood, and the posterior at each grid point. The result (for the entire 20–100 Hz band) is shown in the upper-left panel of Fig. 8. While there is a slight preference for larger values of z_c , no constraint can be placed on this parameter. However, a 95% confidence upper limit on A_{\max} can be placed, $A_{\max}^{95\%} = 2.88 \times 10^{-32} \text{ erg cm}^{-3} \text{ s}^{-1/3}$.

We next add a simulated signal to the measured $\hat{C}_\ell^{\text{cross}}$'s. The simulated signal is computed for $A_{\max} = 2.5 \times 10^{-32} \text{ erg cm}^{-3} \text{ s}^{-1/3}$ and $z_c = 0.6$. We again evaluate the posterior distribution, with the linear grid adjusted to be around these simulated values. The recovery (for the entire 20–100 Hz band) is shown in the lower-left panel of Fig. 8. Note that the simulated parameter point is well within the

recovered two-dimensional 68% and 95% contours, and the one-dimensional distributions include the simulated values within 95% confidence, even though the z_c posterior is not very informative. Hence, our framework successfully recovers the simulated signal in the absence of shot noise.

B. Results with shot noise

Inclusion of shot noise requires two modifications. First, shot noise adds an offset to the angular power spectrum, as in Eq. (2.16). This offset is independent of ℓ , but it is dependent on the astrophysical model parameters θ . Second, the shot noise also modifies the covariance matrix, as in Eq. (5.3). This modification is also dependent on astrophysical parameters θ . Consequently, while shot noise will make harder the recovery of clustering anisotropy, it may actually improve the accuracy for estimation of astrophysical parameters.

As in the no-shot-noise case, we start by computing the posterior distribution in Eq. (6.1) using the measured $\hat{C}_\ell^{\text{cross}}$ and replacing $C_\ell^{\text{cross}}(\theta) \rightarrow C_\ell^{\text{cross,tot}}(\theta)$ and $K_C \rightarrow K_C^{\text{tot}}$ in Eq. (6.2). The results are shown in the upper-right panel of Fig. 8. Again, there is no evidence of signal, even though there is a small (statistically insignificant) preference for higher values of A_{\max} . While the z_c posterior is again not informative, we can place a 95% confidence upper limit on A_{\max} : $A_{\max}^{95\%} = 2.52 \times 10^{-32} \text{ erg cm}^{-3} \text{ s}^{-1/3}$. Note that this upper limit is stronger than in the no-shot-noise case, indicating that addition of shot noise actually improves the sensitivity of this analysis to A_{\max} . The Bayes factor between the model without shot noise and the model with shot noise is 0.475, preferring the inclusion of shot noise.

We next include a simulated signal. In order to keep the shot-noise contribution small (so as to maintain the approximate multivariate Gaussian distribution of $\hat{C}_\ell^{\text{cross}}$'s) we choose 2 times smaller value of $A_{\max} = 1 \times 10^{-32} \text{ erg cm}^{-3} \text{ s}^{-1/3}$ for this simulation. We keep the peak redshift the same as in the no-shot-noise case, $z_c = 0.6$. The lower-right panel of Fig. 8 shows the recovery results. While A_{\max} is not fully resolved at 95% significance, the A_{\max} posterior distribution peaks at $9.0 \times 10^{-33} \text{ erg cm}^{-3} \text{ s}^{-1/3}$, which is consistent with the simulated amplitude. The z_c posterior is still not informative, but it does indicate slight preference for larger values of z_c , consistently with the simulated value of 0.6. We note that the simulated value of A_{\max} is below the 95% upper limit on A_{\max} from the no-shot-noise analysis, indicating that it would not have been observable in the no-shot-noise analysis. This is another indication that inclusion of shot noise in the analysis improves the sensitivity to A_{\max} . The Bayes factor between the model without shot noise and the model with shot noise when we add the same signal of $A_{\max} = 1 \times 10^{-32} \text{ erg cm}^{-3} \text{ s}^{-1/3}$ is 0.428, preferring the inclusion of shot noise.

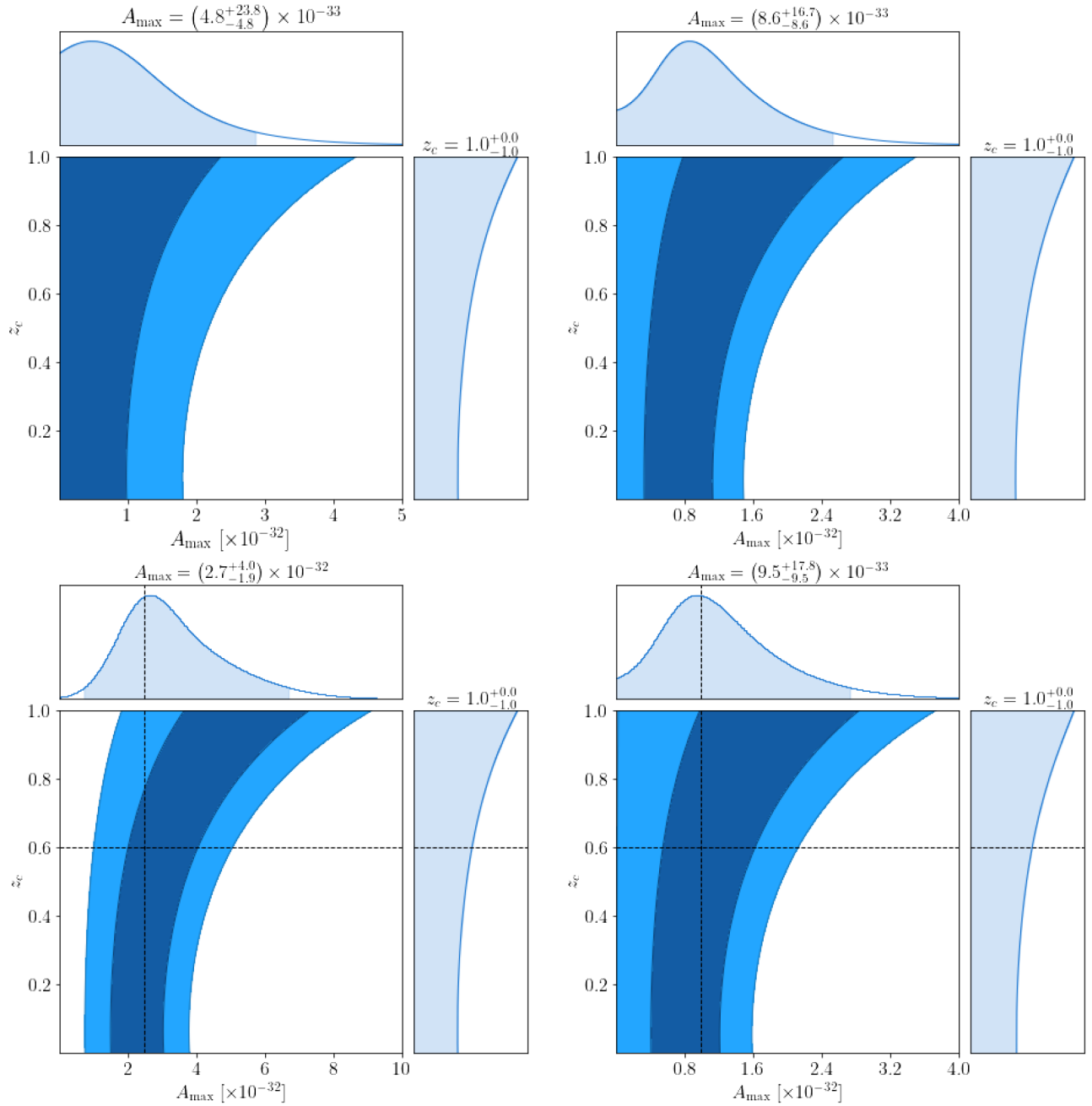


FIG. 8. Results of the parameter estimation for the cross-correlation between the SGWB (20–100 Hz) and the galaxy overdensity from the SDSS spectroscopic catalog plotted using *ChainConsumer* [97]. Each panel shows two-dimensional posterior with 65% and 95% confidence contours, as well as one-dimensional marginalized posteriors with 95% confidence intervals for the two model parameters: A_{\max} in units of $\text{erg cm}^{-3} \text{s}^{-1/3}$ and z_c . Left column panels correspond to the no-shot-noise case, while the right column panels include the shot noise. The upper row panels present upper limits on model parameters (no simulated signal is added). The lower panels show recoveries when a simulated signal is added to the data. The dashed lines indicate the values of simulated parameters. See text for further details.

VII. CONCLUSION AND DISCUSSION

In this paper, we have studied the cross-correlation between the SGWB (as measured in the recent observing runs of Advanced LIGO, Advanced Virgo, and KAGRA) and the distribution of galaxies across the sky measured by

the SDSS survey, and we have extracted for the first time the angular power spectrum of the cross-correlation, in different GW frequency bands. In our study, we assumed that the dominant contribution to the SGWB in the 100 Hz band comes from mergers of extragalactic compact objects. The resulting cross-correlation angular power spectrum is

noise dominated (we do not have a detection yet). However, this spectrum can be compared with predictions from an astrophysical model of the SGWB due to BBH mergers, allowing us to set bounds on model parameters. We assumed that the GW emission is well captured by the quadrupole formula; hence, when modeling the angular power spectrum we could factorize out the frequency dependence. We then introduced a simplified parametrization for the redshift-dependent astrophysical kernel characterizing GW emission at galactic scales: we described this kernel in terms of a global amplitude and a peak position, corresponding to the redshift bin that contributes the most to the total background budget. We explored this 2D parameter space in a Bayesian inference framework, and we found an upper bound for the amplitude of the kernel to be $A_{\max} = 2.52 \times 10^{-32} \text{ erg cm}^{-3} \text{ s}^{-1/3}$ while the peak redshift is left unconstrained. We demonstrated that while including shot noise in the analysis reduces the ability to recover clustering contributions to the anisotropy, it actually improves the sensitivity to the astrophysical kernel parameters. We checked the robustness of our analysis via injection-recovery tests. The Bayes factor comparing the model without shot noise and the model with shot noise is less than 1, showing the preference for inclusion of shot noise.

We stress that in our modeling of the cross-correlation, we assumed that the dominant contribution to the anisotropy comes from clustering; i.e. we assumed that the cross-correlation is dominated by the overdensity term (which we will refer to as $\delta\delta$ term, where δ stands for galaxy overdensity).³ This is a safe assumption in the redshift range $[0, 0.8]$ that we considered in this work and as long as we do not slice it into smaller bins: the clustering term gives indeed the dominant contribution to the anisotropic part of the GW energy density [69]. However, if one wants to take a tomographic approach and try to better reconstruct the redshift dependence of the astrophysical kernel by cross-correlating with a redshift-binned galaxy catalog, some additional care is needed. The reason why is the following: at the angular scales we have access to, the anisotropic part of Ω_{GW} is dominated by contributions of low redshift sources, e.g. sources at $z < 0.1$. Then if we cross-correlate it with galaxies in a low redshift bin (e.g. $z = 0.05$), the dominant contribution in the cross-correlation comes from the clustering ($\delta\delta$) term because the two overdensity terms appearing in the expressions of galaxy number counts and GW energy density have the same support. However, if we correlate with a high redshift bin (e.g. $z = 2$), then the density terms in the two observables do not have the same support. In this case, the dominant contribution to the cross-correlation comes from the (de)magnification term in the galaxy number counts, because it includes contributions of

gravitational potentials integrated along the line of sight [this term corresponds to the κ term in Eq. (13) of [98]]. This term has a minus sign; hence, the $\delta\kappa$ term in the cross-correlation, if dominant, will give rise to an anticorrelation. However, if one integrates the galaxy catalog over redshift, the term $\delta\delta$ (on the redshift range where the two have same support) gives the dominant contribution to the cross-correlation. It follows that considering only clustering is enough for our current purposes.

We stress that the method developed here can be easily adapted and applied to cross-correlations between SGWB and other electromagnetic tracers of structure in the universe. In particular, it can be interesting to perform a joint study of cross-correlation of the SGWB with galaxy counts, weak lensing, CMB, cosmic infrared background, and others. A statistical formalism that enables a joint analysis of these datasets may improve the overall sensitivity of the approach and enable distinguishing different contributions to the BBH SGWB model (e.g. stellar and primordial contributions that may be correlated with different electromagnetic tracers). It would also be interesting to test our pipeline using realistic simulations of the GW sky (simulating the galaxy field and GW emission on galactic scales). Such simulations could enable studies of multiple BBH contributions to the SGWB.

As the sensitivity of the GW detector network improves, the sensitivity of the approach presented here will also improve, enabling more stringent constraints on the astrophysical kernel and its effective parameters. Advanced LIGO, Advanced Virgo, and KAGRA will conduct the fourth observing run in 2023–2025, to be followed with the fifth observing run in 2026–2028. The improved detector sensitivity, extended observation time, and availability of multiple detector pairs for the analysis will improve the sensitivity to $\hat{C}_\ell^{\text{cross}}$ by 20–30 times relative to this work. The next generation of ground-based detectors, such as Einstein Telescope [99] and Cosmic Explorer [100], will enable another ~ 1000 times improvement in sensitivity. Yet another approach could be to use the Bayesian search to estimate the BBH SGWB anisotropy [101], which could also lead to ~ 1000 times sensitivity improvements relative to the approach presented here. These improvements are expected to reach and explore the astrophysically interesting region of the parameter space.

Finally, we note that a significant constraint in this work came from the need to regularize the Fisher matrix in order to invert it. This regularization introduces a potential bias in our analysis, which forced us to constrain the analysis to a relatively small number of spherical harmonics coefficients and to $\ell_{\max} = 5$. There are two ways to remedy this situation in the future. First, availability of more than two GW detectors for this analysis can naturally regularize the Fisher matrix—different baseline pairs have different blind directions, effectively complementing each other and removing the zero eigenvalues of the Fisher matrix.

³In other words, we neglected line of sight effects in the expression of GW overdensity and galaxy number counts; see e.g. [59] for details and derivations.

Second, it may be possible to conduct this analysis using the dirty SGWB sky maps. This approach would avoid inverting the Fisher matrix, but it comes with the challenge of mapping the model C_{ℓ}^{cross} 's into the “dirty space” to enable defining a likelihood function. Studies of this approach are ongoing.

Code and data availability. The gravitational-wave data that support the findings of this study are openly available [102]. The SDSS data are available at the SDSS official Web site, where the photometric catalog (“photoObj”) is under the “imaging data” [103], and the spectroscopic catalog is under the “optical spectra” [104].

ACKNOWLEDGMENTS

This material is based upon work supported by NSF’s LIGO Laboratory, which is a major facility fully funded by the National Science Foundation. The authors are grateful for computational resources provided by the LIGO Laboratory (CIT) supported by National Science Foundation Grants No. PHY-0757058 and No. PHY-0823459, and Inter-University Center for Astronomy and Astrophysics (Sarathi). This research has made use of data or software obtained from the Gravitational Wave Open Science Center, a service of LIGO Laboratory, the LIGO Scientific Collaboration, the Virgo Collaboration, and KAGRA. LIGO Laboratory and Advanced LIGO are funded by the United States National Science Foundation (NSF) as well as the Science and Technology Facilities Council (STFC) of the United Kingdom, the Max-Planck-Society (MPS), and the State of Niedersachsen/Germany for support of the construction of Advanced LIGO and construction and operation of the GEO600 detector. Additional support for Advanced LIGO was provided by the Australian Research Council. Virgo is funded, through the European Gravitational Observatory (EGO), by the French Centre National de Recherche Scientifique (CNRS), the Italian Istituto Nazionale di Fisica Nucleare (INFN) and the Dutch Nikhef, with contributions by institutions from Belgium, Germany, Greece, Hungary,

Ireland, Japan, Monaco, Poland, Portugal, and Spain. The construction and operation of KAGRA are funded by Ministry of Education, Culture, Sports, Science and Technology (MEXT), and Japan Society for the Promotion of Science (JSPS), National Research Foundation (NRF) and Ministry of Science and ICT (MSIT) in Korea, Academia Sinica (AS) and the Ministry of Science and Technology (MoST) in Taiwan. This paper is assigned the LIGO (Laser Interferometer Gravitational-Wave Observatory Laboratory) document control number LIGO-P2200370. The work of G. C. is funded by CNRS and by the Swiss National Foundation “Ambizione” grant *Gravitational wave propagation in the clustered universe*. We are very grateful to David Alonso and Fabien Lacasa for interesting exchanges and discussions during this project. J. S. is supported by an Actions de Recherche Concertées (ARC) grant. K. Z. Y., S. B., V. M., and C. S. were in part supported by NSF Grant No. PHY-2011675. The authors thank Leo Tsukada for carefully reading the manuscript and providing valuable comments.

APPENDIX: PARAMETER ESTIMATION IN 10 HZ FREQUENCY BINS

We present parameter estimation results in each 10-Hz-wide frequency bin from 20 to 100 Hz (labeled by their center frequency) in the following figures: upper limits of parameters without and with shot noise effects (Figs. 9 and 11, respectively); injection recovery without and with shot noise effects (Figs. 10 and 12, respectively). For Fig. 10, we simulated the signal with $A_{\text{max}} = 2.5 \times 10^{-32} \text{ erg cm}^{-3} \text{ s}^{-1/3}$ and $z_c = 0.6$. For Fig. 12, we simulated the signal with $A_{\text{max}} = 1 \times 10^{-32} \text{ erg cm}^{-3} \text{ s}^{-1/3}$ and $z_c = 0.6$. While the recovered contours are still consistent with the simulated parameter values, the contours are rather large due to the smallness of the simulated A_{max} . Combining all frequency bands gives a much stronger estimate of A_{max} as shown in the lower-right panel of Fig. 8.

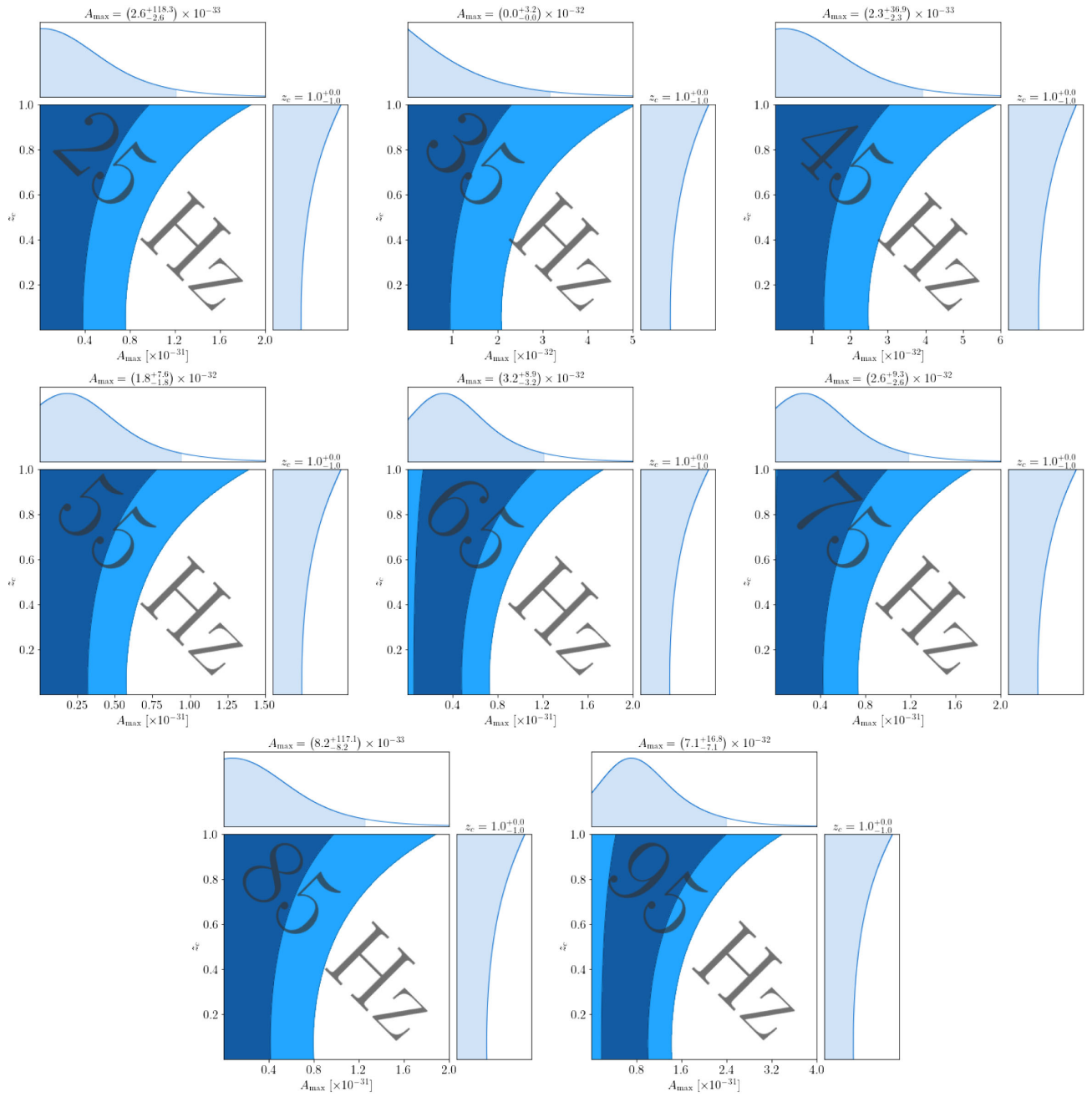


FIG. 9. Upper limits of parameters A_{\max} in units of $\text{erg cm}^{-3} \text{s}^{-1/3}$ and z_c for SGWB measured in different frequency bands, without including the shot noise.

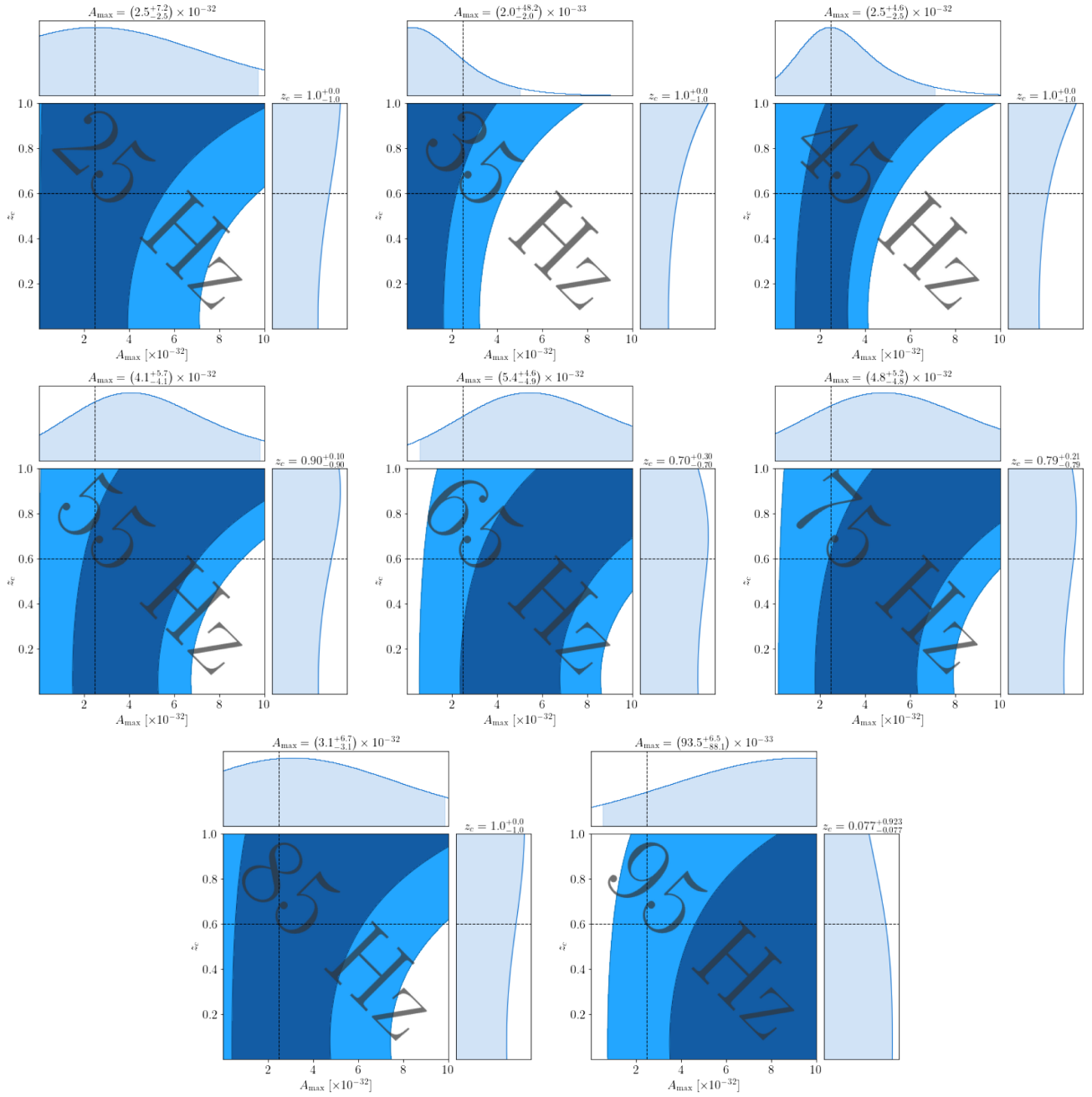


FIG. 10. Recovery of a simulated signal with parameters $A_{\max} = 2.5 \times 10^{-32}$ erg cm $^{-3}$ s $^{-1/3}$ and $z_c = 0.6$, using SGWB measured in different frequency bands and without including shot noise.

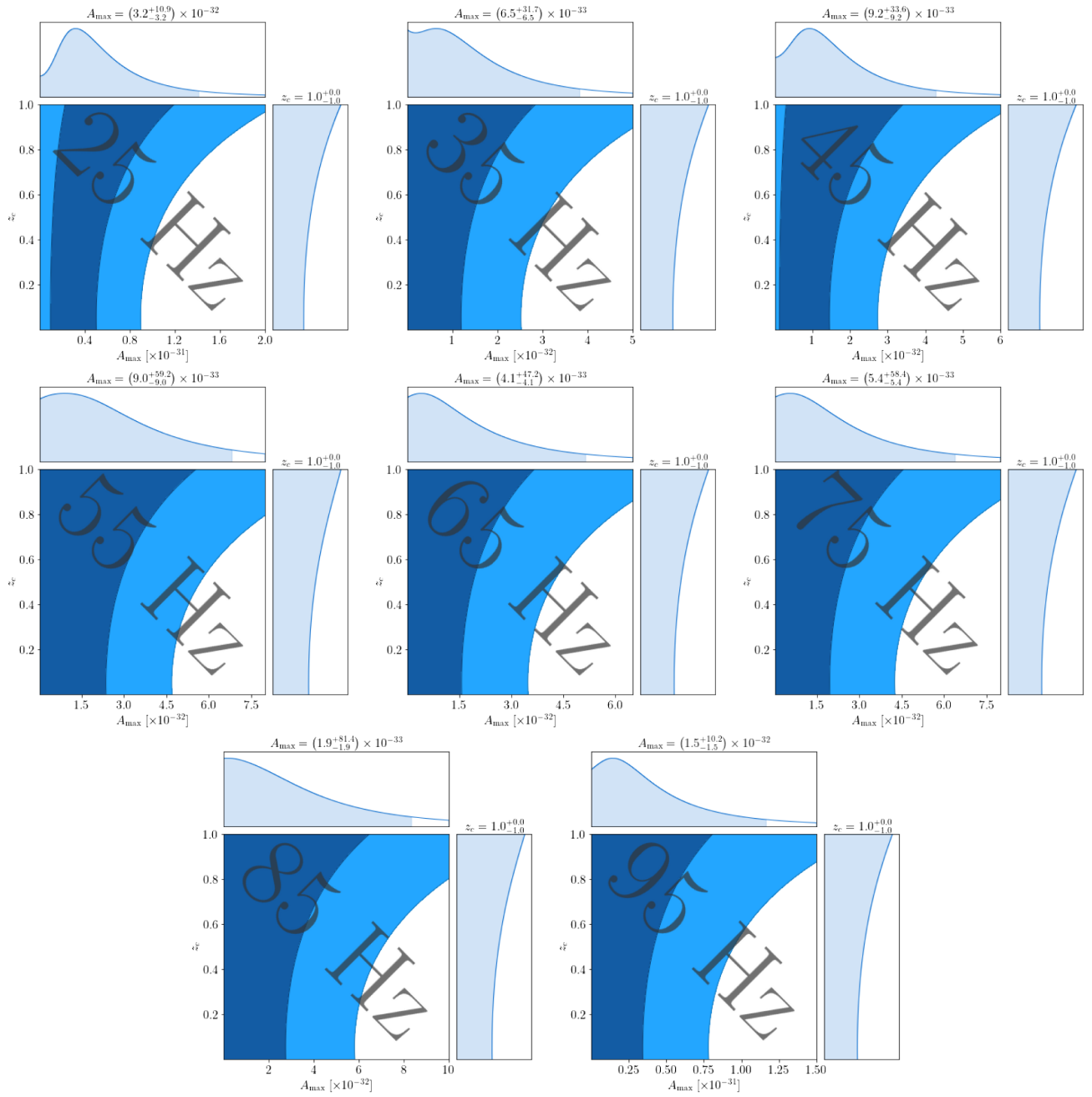


FIG. 11. Upper limits on parameters A_{\max} in units of $\text{erg cm}^{-3} \text{s}^{-1/3}$ and z_c for SGWB measured in different frequency bands, including the shot noise.

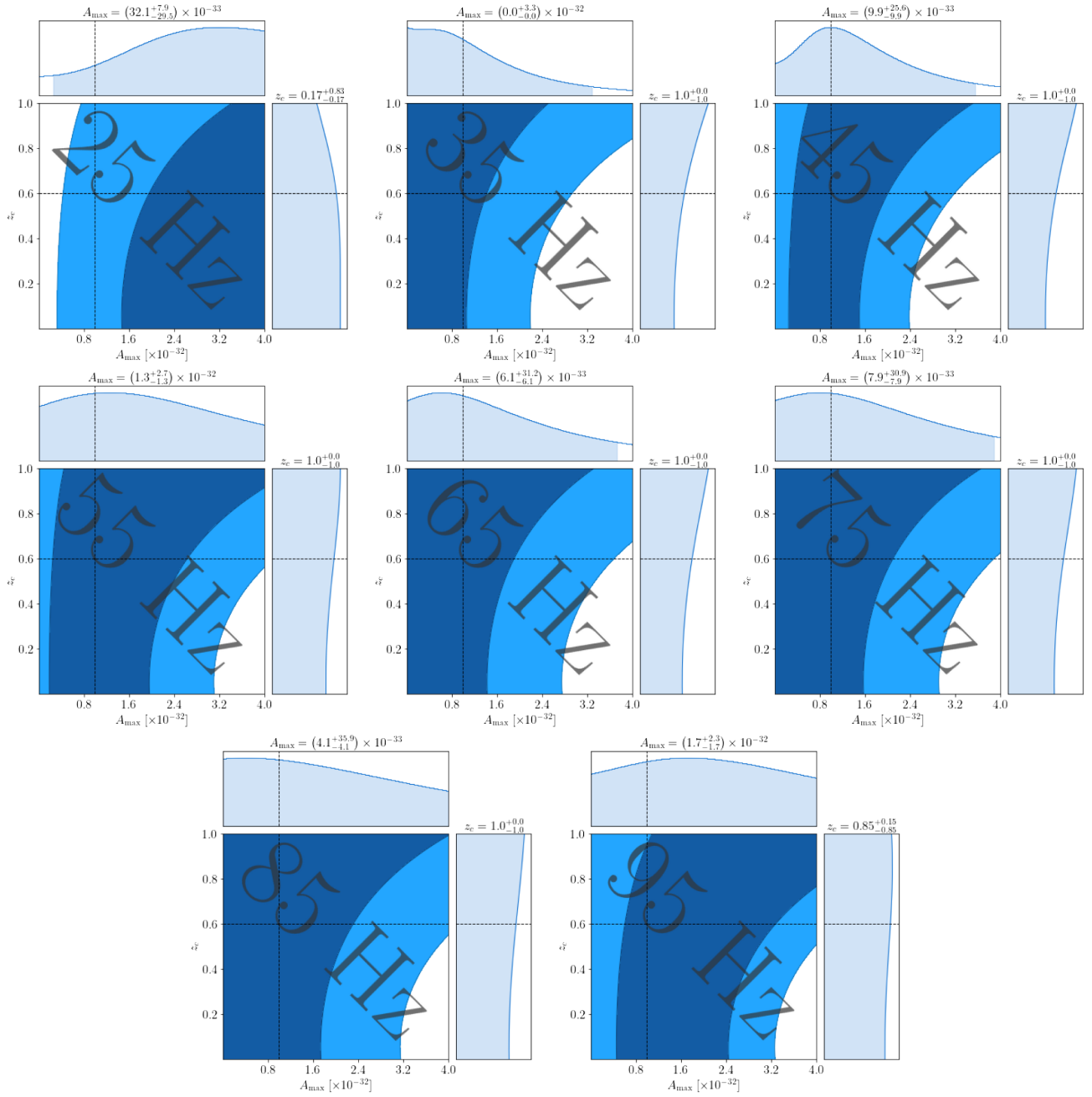


FIG. 12. Recovery of a simulated signal with parameters $A_{\max} = 1 \times 10^{-32} \text{ erg cm}^{-3} \text{ s}^{-1/3}$ and $z_c = 0.6$, using SGWB measured in different frequency bands and including shot noise.

- [1] LIGO Scientific Collaboration, Advanced LIGO, *Classical Quantum Gravity* **32**, 074001 (2015).
- [2] F. Acernese *et al.*, Advanced Virgo: A second-generation interferometric gravitational wave detector, *Classical Quantum Gravity* **32**, 024001 (2015).
- [3] T. Akutsu *et al.* (KAGRA Collaboration), Overview of KAGRA: Calibration, detector characterization, physical environmental monitors, and the geophysics interferometer, *Prog. Theor. Exp. Phys.* **2021**, 05A102 (2021).
- [4] R. Abbott *et al.*, GWTC-3: Compact Binary Coalescences Observed by LIGO and Virgo During the Second Part of the Third Observing Run, [arXiv:2111.03606](https://arxiv.org/abs/2111.03606).
- [5] R. Abbott *et al.*, The Population of Merging Compact Binaries Inferred Using Gravitational Waves Through GWTC-3, *Phys. Rev. X* **13**, 011048 (2023).
- [6] R. Abbott *et al.*, Tests of general relativity with GWTC-3, [arXiv:2112.06861](https://arxiv.org/abs/2112.06861).
- [7] R. Abbott *et al.*, Constraints on the cosmic expansion history from GWTC-3, *Astrophys. J.* **949**, 76 (2023).
- [8] B. P. Abbott *et al.* (LIGO Scientific Collaboration and the Virgo Collaboration), GW170817: Measurements of Neutron Star Radii and Equation of State, *Phys. Rev. Lett.* **121**, 161101 (2018).
- [9] B. Abbott *et al.*, Prospects for observing and localizing gravitational-wave transients with Advanced LIGO, Advanced Virgo and KAGRA, *Living Rev. Relativity* **23**, 3 (2020).
- [10] M. Maggiore, Gravitational wave experiments and early universe cosmology, *Phys. Rep.* **331**, 283 (2000).
- [11] T. Regimbau, The astrophysical gravitational wave stochastic background, *Res. Astron. Astrophys.* **11**, 369 (2011).
- [12] L. P. Grishchuk, The amplification of gravitational waves and creation of gravitons in the isotropic universes, *Lett. Nuovo Cimento* **12**, 60 (1975).
- [13] R. Bar-Kana, Limits on direct detection of gravitational waves, *Phys. Rev. D* **50**, 1157 (1994).
- [14] A. A. Starobinskiĭ, Spectrum of relict gravitational radiation and the early state of the universe, *Sov. J. Exp. Theor. Phys. Lett.* **30**, 682 (1979).
- [15] M. S. Turner, Detectability of inflation-produced gravitational waves, *Phys. Rev. D* **55**, R435 (1997).
- [16] N. Barnaby, E. Pajer, and M. Peloso, Gauge field production in axion inflation: Consequences for monodromy, non-Gaussianity in the CMB, and gravitational waves at interferometers, *Phys. Rev. D* **85**, 023525 (2012).
- [17] N. Seto and A. Taruya, Measuring a Parity-Violation Signature in the Early Universe via Ground-Based Laser Interferometers, *Phys. Rev. Lett.* **99**, 121101 (2007).
- [18] R. Easther and E. A. Lim, Stochastic gravitational wave production after inflation, *J. Cosmol. Astropart. Phys.* **04** (2006) 010.
- [19] L. A. Boyle and A. Buonanno, Relating gravitational wave constraints from primordial nucleosynthesis, pulsar timing, laser interferometers, and the CMB: Implications for the early universe, *Phys. Rev. D* **78**, 043531 (2008).
- [20] E. Witten, Cosmic separation of phases, *Phys. Rev. D* **30**, 272 (1984).
- [21] C. J. Hogan, Gravitational radiation from cosmological phase transitions, *Mon. Not. R. Astron. Soc.* **218**, 629 (1986).
- [22] A. Kosowsky, M. S. Turner, and R. Watkins, Gravitational Waves from First-Order Cosmological Phase Transitions, *Phys. Rev. Lett.* **69**, 2026 (1992).
- [23] C. Caprini, R. Durrer, and G. Servant, Gravitational wave generation from bubble collisions in first-order phase transitions: An analytic approach, *Phys. Rev. D* **77**, 124015 (2008).
- [24] P. Binétruy, A. Bohé, C. Caprini, and J.-F. Dufaux, Cosmological backgrounds of gravitational waves and eLISA/NGO: Phase transitions, cosmic strings and other sources, *J. High Energy Phys.* **06** (2012) 027.
- [25] C. Caprini *et al.*, Science with the space-based interferometer eLISA. II: Gravitational waves from cosmological phase transitions, *J. High Energy Phys.* **04** (2016) 001.
- [26] M. Fitz Axen, S. Banagiri, A. Matas, C. Caprini, and V. Mandic, Multiwavelength observations of cosmological phase transitions using LISA and cosmic explorer, *Phys. Rev. D* **98**, 103508 (2018).
- [27] R. R. Caldwell and B. Allen, Cosmological constraints on cosmic-string gravitational radiation, *Phys. Rev. D* **45**, 3447 (1992).
- [28] T. Damour and A. Vilenkin, Gravitational Wave Bursts from Cosmic Strings, *Phys. Rev. Lett.* **85**, 3761 (2000).
- [29] T. Damour and A. Vilenkin, Gravitational radiation from cosmic (super)strings: Bursts, stochastic background, and observational windows, *Phys. Rev. D* **71**, 063510 (2005).
- [30] X. Siemens, V. Mandic, and J. Creighton, Gravitational-Wave Stochastic Background from Cosmic Strings, *Phys. Rev. Lett.* **98**, 111101 (2007).
- [31] S. Ölmez, V. Mandic, and X. Siemens, Gravitational-wave stochastic background from kinks and cusps on cosmic strings, *Phys. Rev. D* **81**, 104028 (2010).
- [32] E. J. Copeland, R. C. Myers, and J. Polchinski, Cosmic F- and D-strings, *J. High Energy Phys.* **06** (2004) 013.
- [33] X. Siemens, J. Creighton, I. Maor, S. R. Majumder, K. Cannon, and J. Read, Gravitational wave bursts from cosmic (super)strings: Quantitative analysis and constraints, *Phys. Rev. D* **73**, 105001 (2006).
- [34] L. Lorenz, C. Ringeval, and M. Sakellariadou, Cosmic string loop distribution on all length scales and at any redshift, *J. High Energy Phys.* **10** (2010) 003.
- [35] J. J. Blanco-Pillado, K. D. Olum, and B. Shlaer, Number of cosmic string loops, *Phys. Rev. D* **89**, 023512 (2014).
- [36] R. Abbott *et al.* (LIGO Scientific Collaboration, Virgo Collaboration, and KAGRA Collaboration), Constraints on Cosmic Strings Using Data from the Third Advanced LIGO–Virgo Observing Run, *Phys. Rev. Lett.* **126**, 241102 (2021).
- [37] A. C. Jenkins and M. Sakellariadou, Anisotropies in the stochastic gravitational-wave background: Formalism and the cosmic string case, *Phys. Rev. D* **98**, 063509 (2018).
- [38] T. Regimbau and J. A. de Freitas Pacheco, Stochastic background from coalescences of neutron star–neutron star binaries, *Astrophys. J.* **642**, 455 (2006).
- [39] X.-J. Zhu, E. Howell, T. Regimbau, D. Blair, and Z.-H. Zhu, Stochastic gravitational wave background from coalescing binary black holes, *Astrophys. J.* **739**, 86 (2011).
- [40] S. Marassi, R. Schneider, G. Corvino, V. Ferrari, and S. P. Zwart, Imprint of the merger and ring-down on the

- gravitational wave background from black hole binaries coalescence, *Phys. Rev. D* **84**, 124037 (2011).
- [41] P. A. Rosado, Gravitational wave background from binary systems, *Phys. Rev. D* **84**, 084004 (2011).
- [42] T. Regimbau and V. Mandic, Astrophysical sources of a stochastic gravitational-wave background, *Classical Quantum Gravity* **25**, 184018 (2008).
- [43] C. Wu, V. Mandic, and T. Regimbau, Accessibility of the gravitational-wave background due to binary coalescences to second and third generation gravitational-wave detectors, *Phys. Rev. D* **85**, 104024 (2012).
- [44] B. P. Abbott *et al.* (LIGO Scientific Collaboration and Virgo Collaboration), GW150914: Implications for the Stochastic Gravitational-Wave Background from Binary Black Holes, *Phys. Rev. Lett.* **116**, 131102 (2016).
- [45] B. P. Abbott *et al.*, GW170817: Implications for the Stochastic Gravitational-Wave Background from Compact Binary Coalescences, *Phys. Rev. Lett.* **120**, 091101 (2018).
- [46] C. Cutler, Gravitational waves from neutron stars with large toroidal B fields, *Phys. Rev. D* **66**, 084025 (2002).
- [47] S. Bonazzola and E.ourgoulhon, Gravitational waves from pulsars: Emission by the magnetic field induced distortion, *Astron. Astrophys.* **312**, 675 (1996), <https://adsabs.harvard.edu/full/1996A%26A...312..675B>.
- [48] S. Marassi, R. Ciolfi, R. Schneider, L. Stella, and V. Ferrari, Stochastic background of gravitational waves emitted by magnetars, *Mon. Not. R. Astron. Soc.* **411**, 2549 (2011).
- [49] B. J. Owen, L. Lindblom, C. Cutler, B. F. Schutz, A. Vecchio, and N. Andersson, Gravitational waves from hot young rapidly rotating neutron stars, *Phys. Rev. D* **58**, 084020 (1998).
- [50] C.-J. Wu, V. Mandic, and T. Regimbau, Accessibility of the stochastic gravitational wave background from magnetars to the interferometric gravitational wave detectors, *Phys. Rev. D* **87**, 042002 (2013).
- [51] D. M. Coward, R. R. Burman, and D. G. Blair, Simulating a stochastic background of gravitational waves from neutron star formation at cosmological distances, *Mon. Not. R. Astron. Soc.* **329**, 411 (2002).
- [52] S. Marassi, R. Schneider, and V. Ferrari, Gravitational wave backgrounds and the cosmic transition from Population III to Population II stars, *Mon. Not. R. Astron. Soc.* **398**, 293 (2009).
- [53] P. Sandick, K. A. Olive, F. Daigne, and E. Vangioni, Gravitational waves from the first stars, *Phys. Rev. D* **73**, 104024 (2006).
- [54] A. Buonanno, G. Sigl, G. G. Raffelt, H.-T. Janka, and E. Muller, Stochastic gravitational-wave background from cosmological supernovae, *Phys. Rev. D* **72**, 084001 (2005).
- [55] K. Crocker, V. Mandic, T. Regimbau, K. Belczynski, W. Gladysz, K. Olive, T. Prestegard, and E. Vangioni, Model of the stochastic gravitational-wave background due to core collapse to black holes, *Phys. Rev. D* **92**, 063005 (2015).
- [56] K. Crocker, T. Prestegard, V. Mandic, T. Regimbau, K. Olive, and E. Vangioni, Systematic study of the stochastic gravitational-wave background due to stellar core collapse, *Phys. Rev. D* **95**, 063015 (2017).
- [57] B. Finkel, H. Andresen, and V. Mandic, Stochastic gravitational-wave background from stellar core-collapse events, *Phys. Rev. D* **105**, 063022 (2022).
- [58] C. R. Contaldi, Anisotropies of gravitational wave backgrounds: A line of sight approach, *Phys. Lett. B* **771**, 9 (2017).
- [59] G. Cusin, C. Pitrou, and J.-P. Uzan, Anisotropy of the astrophysical gravitational wave background: Analytic expression of the angular power spectrum and correlation with cosmological observations, *Phys. Rev. D* **96**, 103019 (2017).
- [60] G. Cusin, C. Pitrou, and J.-P. Uzan, The signal of the gravitational wave background and the angular correlation of its energy density, *Phys. Rev. D* **97**, 123527 (2018).
- [61] G. Cusin and G. Tasinato, Doppler boosting the stochastic gravitational wave background, *J. Cosmol. Astropart. Phys.* **08** (2022) 036.
- [62] A. K.-W. Chung, A. C. Jenkins, J. D. Romano, and M. Sakellariadou, Targeted search for the kinematic dipole of the gravitational-wave background, *Phys. Rev. D* **106**, 082005 (2022).
- [63] M. Geller, A. Hook, R. Sundrum, and Y. Tsai, Primordial Anisotropies in the Gravitational Wave Background from Cosmological Phase Transitions, *Phys. Rev. Lett.* **121**, 201303 (2018).
- [64] G. Cusin, I. Dvorkin, C. Pitrou, and J.-P. Uzan, First Predictions of the Angular Power Spectrum of the Astrophysical Gravitational Wave Background, *Phys. Rev. Lett.* **120**, 231101 (2018).
- [65] G. Cusin, I. Dvorkin, C. Pitrou, and J.-P. Uzan, Properties of the stochastic astrophysical gravitational wave background: Astrophysical sources dependencies, *Phys. Rev. D* **100**, 063004 (2019).
- [66] A. C. Jenkins, M. Sakellariadou, T. Regimbau, and E. Slezak, Anisotropies in the astrophysical gravitational-wave background: Predictions for the detection of compact binaries by LIGO and Virgo, *Phys. Rev. D* **98**, 063501 (2018).
- [67] A. C. Jenkins, R. O'Shaughnessy, M. Sakellariadou, and D. Wysocki, Anisotropies in the Astrophysical Gravitational-Wave Background: The Impact of Black Hole Distributions, *Phys. Rev. Lett.* **122**, 111101 (2019).
- [68] A. C. Jenkins and M. Sakellariadou, Anisotropies in the stochastic gravitational-wave background: Formalism and the cosmic string case, *Phys. Rev. D* **98**, 063509 (2018).
- [69] G. Cusin, I. Dvorkin, C. Pitrou, and J.-P. Uzan, Stochastic gravitational wave background anisotropies in the mHz band: Astrophysical dependencies, *Mon. Not. R. Astron. Soc.* **493**, L1 (2020).
- [70] A. C. Jenkins and M. Sakellariadou, Shot noise in the astrophysical gravitational-wave background, *Phys. Rev. D* **100**, 063508 (2019).
- [71] A. C. Jenkins, J. D. Romano, and M. Sakellariadou, Estimating the angular power spectrum of the gravitational-wave background in the presence of shot noise, *Phys. Rev. D* **100**, 083501 (2019).
- [72] G. Cusin, R. Durrer, and P. G. Ferreira, Polarization of a stochastic gravitational wave background through diffusion by massive structures, *Phys. Rev. D* **99**, 023534 (2019).
- [73] C. Pitrou, G. Cusin, and J. P. Uzan, Unified view of anisotropies in the astrophysical gravitational-wave background, *Phys. Rev. D* **101**, 081301(R) (2020).

- [74] D. Alonso, G. Cusin, P.G. Ferreira, and C. Pitrou, Detecting the anisotropic astrophysical gravitational wave background in the presence of shot noise through cross-correlations, *Phys. Rev. D* **102**, 023002 (2020).
- [75] K.Z. Yang, V. Mandic, C. Scarlata, and S. Banagiri, Searching for cross-correlation between stochastic gravitational wave background and galaxy number counts, *Mon. Not. R. Astron. Soc.* **500**, 1666 (2020).
- [76] G. Capurri, A. Lapi, C. Baccigalupi, L. Boco, G. Scelfo, and T. Ronconi, Intensity and anisotropies of the stochastic gravitational wave background from merging compact binaries in galaxies, *J. Cosmol. Astropart. Phys.* **11** (2021) 032.
- [77] S. Mukherjee, A. Krolewski, B.D. Wandelt, and J. Silk, Cross-correlating dark sirens and galaxies: measurement of H_0 from GWTC-3 of LIGO-Virgo-KAGRA, [arXiv:2203.03643](https://arxiv.org/abs/2203.03643).
- [78] F.A. Marin *et al.* (WiggleZ Collaboration), The WiggleZ dark energy survey: Constraining galaxy bias and cosmic growth with 3-point correlation functions, *Mon. Not. R. Astron. Soc.* **432**, 2654 (2013).
- [79] A. Rassat, A. Amara, L. Amendola, F.J. Castander, T. Kitching, M. Kunz, A. Refregier, Y. Wang, and J. Weller, Deconstructing baryon acoustic oscillations: A comparison of methods, [arXiv:0810.0003](https://arxiv.org/abs/0810.0003).
- [80] A. Ain, P. Dalvi, and S. Mitra, Fast gravitational wave radiometry using data folding, *Phys. Rev. D* **92**, 022003 (2015).
- [81] L.S. Collaboration, V. Collaboration, and K. Collaboration, Folded data for first three observing runs of Advanced LIGO and Advanced Virgo, [10.5281/zenodo.6326656](https://doi.org/10.5281/zenodo.6326656) (2022).
- [82] N. Aghanim *et al.*, Planck 2018 results. VI. Cosmological parameters, *Astron. Astrophys.* **641**, A6 (2020).
- [83] E. Thrane, S. Ballmer, J.D. Romano, S. Mitra, D. Talukder, S. Bose, and V. Mandic, Probing the anisotropies of a stochastic gravitational-wave background using a network of ground-based laser interferometers, *Phys. Rev. D* **80**, 122002 (2009).
- [84] J.D. Romano and N.J. Cornish, Detection methods for stochastic gravitational-wave backgrounds: A unified treatment, *Living Rev. Relativity* **20**, 2 (2017).
- [85] S. Mitra, S. Dhurandhar, T. Souradeep, A. Lazzarini, V. Mandic, S. Bose, and S. Ballmer, Gravitational wave radiometry: Mapping a stochastic gravitational wave background, *Phys. Rev. D* **77**, 042002 (2008).
- [86] B. Allen and J.D. Romano, Detecting a stochastic background of gravitational radiation: Signal processing strategies and sensitivities, *Phys. Rev. D* **59**, 102001 (1999).
- [87] S. Panda, S. Bhagwat, J. Suresh, and S. Mitra, Stochastic gravitational wave background mapmaking using regularized deconvolution, *Phys. Rev. D* **100**, 043541 (2019).
- [88] D. Agarwal, J. Suresh, S. Mitra, and A. Ain, Upper limits on persistent gravitational waves using folded data and the full covariance matrix from Advanced LIGO's first two observing runs, *Phys. Rev. D* **104**, 123018 (2021).
- [89] E. Floden, V. Mandic, A. Matas, and L. Tsukada, Angular resolution of the search for anisotropic stochastic gravitational-wave background with terrestrial gravitational-wave detectors, *Phys. Rev. D* **106**, 023010 (2022).
- [90] A. Ain, J. Suresh, and S. Mitra, Very fast stochastic gravitational wave background map making using folded data, *Phys. Rev. D* **98**, 024001 (2018).
- [91] J. Suresh, A. Ain, and S. Mitra, Unified mapmaking for an anisotropic stochastic gravitational wave background, *Phys. Rev. D* **103**, 083024 (2021).
- [92] R. Abbott, T.D. Abbott *et al.* (LIGO Scientific Collaboration, Virgo Collaboration, and KAGRA Collaboration), Search for anisotropic gravitational-wave backgrounds using data from Advanced LIGO and Advanced Virgo's first three observing runs, *Phys. Rev. D* **104**, 022005 (2021).
- [93] D. Agarwal, J. Suresh, S. Mitra, and A. Ain, Angular power spectra of anisotropic stochastic gravitational wave background: Developing statistical methods and analyzing data from ground-based detectors, *Phys. Rev. D* **108**, 023011 (2023).
- [94] R. Ahumada *et al.*, The 16th data release of the sloan digital sky surveys: First release from the APOGEE-2 southern survey and full release of eBOSS spectra, *Astrophys. J. Suppl. Ser.* **249**, 3 (2020).
- [95] K.M. Gorski, B.D. Wandelt, F.K. Hansen, E. Hivon, and A.J. Banday, The HEALPix primer, [arXiv:astro-ph/9905275](https://arxiv.org/abs/astro-ph/9905275).
- [96] D. Alonso, C.R. Contaldi, G. Cusin, P.G. Ferreira, and A.I. Renzini, Noise angular power spectrum of gravitational wave background experiments, *Phys. Rev. D* **101**, 124048 (2020).
- [97] S. Hinton, ChainConsumer, *J. Open Source Softw.* **1**, 00045 (2016).
- [98] M. Bruni, R. Crittenden, K. Koyama, R. Maartens, C. Pitrou, and D. Wands, Disentangling non-Gaussianity, bias and GR effects in the galaxy distribution, *Phys. Rev. D* **85**, 041301(R) (2012).
- [99] M. Punturo *et al.*, The Einstein telescope: A third-generation gravitational wave observatory, *Classical Quantum Gravity* **27**, 194002 (2010).
- [100] B. Abbott *et al.*, Exploring the sensitivity of next generation gravitational wave detectors, *Classical Quantum Gravity* **34**, 044001 (2017).
- [101] S. Banagiri, V. Mandic, C. Scarlata, and K.Z. Yang, Measuring angular N-point correlations of binary black-hole merger gravitational-wave events with hierarchical Bayesian inference, *Phys. Rev. D* **102**, 063007 (2020).
- [102] [10.5281/zenodo.6326656](https://doi.org/10.5281/zenodo.6326656).
- [103] <https://www.sdss.org/dr16/imaging/catalogs/>.
- [104] <https://www.sdss.org/dr16/spectro/>.